Using X-ray Colour-Colour Diagrams to Study AGN Variability

by

Ben Pottie

A THESIS SUBMITTED IN PARTIAL FULFILMENT OF
THE REQUIREMENTS FOR THE DEGREE OF

BACHELOR OF SCIENCE

in

Honours Astrophysics

(Department of Astronomy and Physics)

. . . .
. . . .
. . . .
. . . .
. . . .

SAINT MARY'S UNIVERSITY

May 6, 2022

Acknowledgement

I would like to thank Dr Luigi Gallo, my supervisor, for providing help and making sure I stayed on track throughout the year. Additionally, I would like to thank Adam Gonzalez for always being able to point me in the right direction when difficulties arose during data gathering. Another thanks goes out to the both of them for making sure that this was a true learning experience for me, and to the SMASHERS research group for their continuous support.

Abstract

Using X-ray Colour-Colour Diagrams to Study AGN Variability

by *Ben Pottie*

Identifying X-ray variability in active galactic nuclei (AGN) has been a longstanding issue due to spectral model degeneracies. It often occurs on timescales too short to employ regular spectral analysis, but colour-colour analysis provides a unique opportunity to get past this problem. Studies like in Grinberg et al. (2020) have shown the application of colour-colour diagrams to high-mass X-ray binary variability for determining partial absorber properties. Colour-colour diagrams were generated for absorbed power law, partial covering, and relativistic blurred reflection models to assess parameter variability. Comparisons were done with both simulated data sets, and real data from an observation of NGC 6814. The use of simulated data demonstrated that these diagrams have the ability to predict parameter changes, but can have difficulties distinguishing between parameter variations. Real data showed that grids need to have more consistency to accurately compare to real data and predict correct parameter changes. Some consistency was seen when comparing to current analyses on NGC 6814, but it warrants further studies. Colour-colour diagrams have shown promise, and future detailed works involving the inclusion of other components, should be quite useful.

May 6, 2022

Contents

List of Figures

Chapter 1

INTRODUCTION

1.1 WHAT ARE ACTIVE GALACTIC NUCLEI (AGN)?

1.1.1 CLASSIFYING AGN

A majority of galaxies are believed to have a supermassive black hole (SMBH) at their center. They can have a large variety of sizes and tend to have masses in the range of millions to even billions of times the mass of the Sun. In comparison to the total mass of stellar objects in a galaxy, these SMBHs only make up about 0.3% of that total. Some of these galaxies, only a small percentage, are considered Active Galactic Nuclei (AGN). These are considered "active" as they interact largely with their surroundings mainly through the process of accretion, where material is pulled towards the central black hole due to its strong gravitational influence. This can lead to radiation processes that allow it to produce some of the highest luminosities in the known universe, and it is especially efficient at doing so (up to 40% efficiency). They are able to emit over the entire electromagnetic spectrum, but we choose to mainly focus on X-rays, as they are highly variable in this energy range. This emission comes from regions closest to the SMBH, so studying X-ray emission also allows us to better

understand this inner region (Gallo, 2011).

A quality of AGN that is not present in a normal galaxy is the potential for some to produce jets, which are highly ionized gas propelled at relativistic speeds that are mainly produced from magnetic fields interacting with the highly spinning black hole (Blandford et al., 2018). The main difference between active and normal galaxies is that active galaxies have their light dominated from the radiation processes occurring in this galactic center, while normal galaxies have their light dominated by the collective luminosity of all the stars radiating within the galaxy (Gallo, 2011). Thus, the spectra of normal galaxies tend to have a blackbody dominated shape, while the spectra of active galaxies tend to have a more power law dominated shape, as can be seen in Figure 1.1. Even though a large percentage of galaxies are not considered active, there still exists a great deal of AGN that we can analyze, which helps us to learn about the various processes that do occur at galactic centers.

There are a few components that make up AGN. These components are the SMBH and accretion disc, which form the central engine, along with a hot electron corona, a dusty torus, and both a broad line region and a narrow line region (Ehler et al., 2018). The central SMBH is what material accretes into and is the main driver of the X-ray emission. As gravity causes material to fall towards the black hole, a spiralling disc of material called the accretion disc is formed. The disc is generally sustained in its spiral through angular momentum transfer from the inner parts of the disc, which have higher angular momentum, to the outer parts through friction as the different parts of the disc are travelling with different velocities (Gallo, 2011). Generally, the disc is made up of optically thick hot gas and is treated as radiating like a blackbody
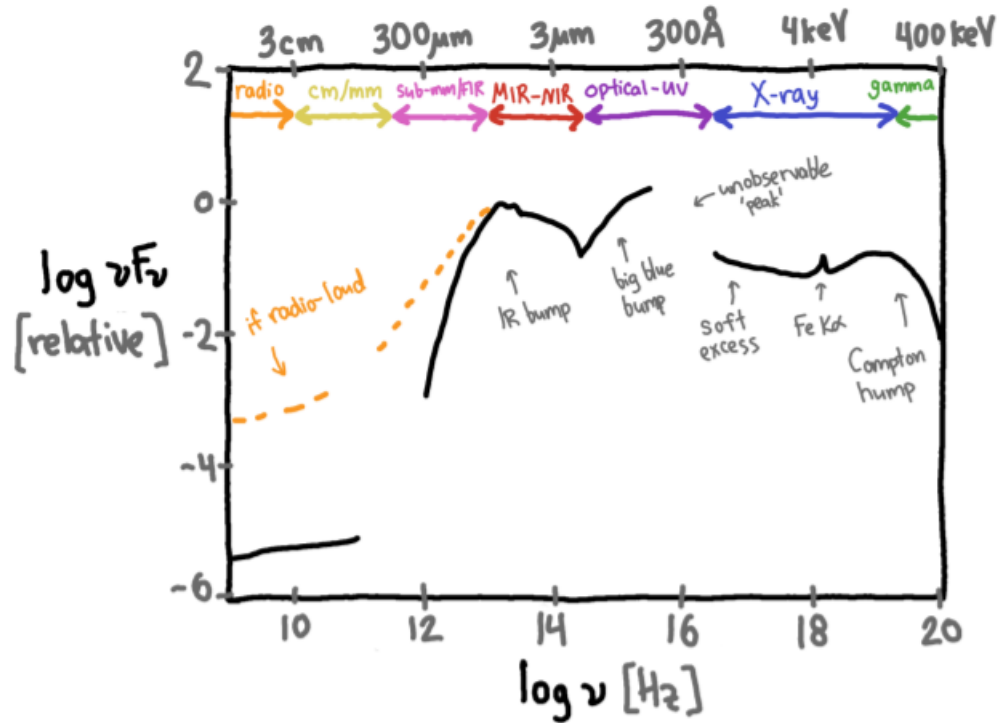
Figure 1.1: Depiction of the Spectral Energy Distribution (SED) for an AGN with various key parts of the distribution labelled. Taken from Ehler, 2019.

(Tanaka et al., 2004). There are other more complex models that are used to explain its emission, but the simpler model is sufficient here.

The main component responsible for the X-rays is the electron corona, a cloud of hot, fast electrons that can reach temperatures up to around $10^9 K$. It is believed to be formed through electrons being removed from deep in the accretion disc through magnetic field reconnection, much like the solar corona is formed around the Sun. Changes in magnetic field lines as they constantly reconnect cause changes in electron trajectory that deposit them in this different region (Gallo, 2011). Corona geometry is not super well known, but there are some main ideas for what exactly it could be. Models for the orientation and geometry of AGN indicate that the corona is likely above the accretion disk at some height, but more studies are necessary to pinpoint

the exact location (Ehler et al., 2018). Usually we tend to consider the "lamppost model" for describing the corona, which treats the corona like a point source situated directly above the black hole spin axis, as in the configuration of Figure 1.2.

There are various possibilities for a more complex corona geometry that are currently being analyzed, which often involve considering it being patchy (i.e., non-uniform electron density throughout the corona) or collimated (i.e., parallel rays of electrons). It is likely to be constantly changing throughout various timescales, meaning that it should be quite dynamic, which would make sense with how much this component interacts with other AGN components. It is also thought that it could be extended, which usually means that the corona would be much larger and more spread out so that it covers a region above the spin axis along with some portion of the inner accretion disc region. Moreover, extended geometries indicate a system where point sources are distributed throughout a region. This can be in a cylindrical form (a cylindrical slab off electrons above the BH spin axis), a spheroidal form (consists of hemisphere of electrons surrounding the black hole and a portion of the inner disk), or a conical form (a cone of coronal electrons expanding out as the height above BH increases) (Gonzalez et al., 2017).

The dusty torus is a ring that is optically thick and consists of hot gas and dust and is located outside of the accretion disc, meaning that it can obscure a large amount of radiation from the central engine depending on our viewing angle (Ehler et al., 2018). In the region interior to the dusty torus (i.e., around the central engine region) lies what we call the broad line region (BLR). Optical emission lines emitted from the region are Doppler broadened. Exterior to the dusty torus, on galactic scales, lies
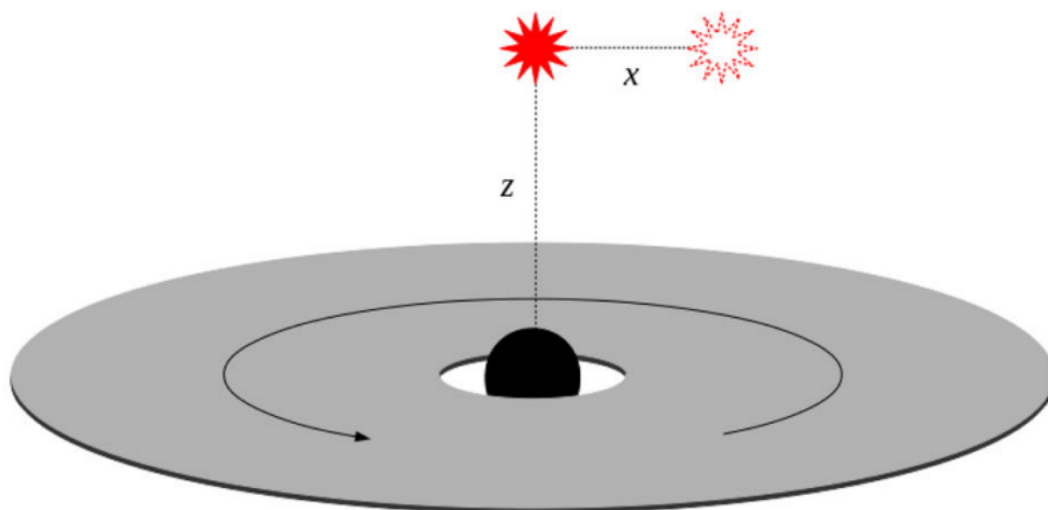
Figure 1.2: Depicted here is the "lamppost" model for an AGN corona. The point source is located at a height z above the black hole and displaced a distance x from the spin axis. Taken from Gonzalez et al., 2017.

the narrow line region (NLR). Emission lines from the NLR are narrow as they are dominated by the gravitational potential of the surrounding stars. However, since the NLR is ionized by the central engine, it is considered an AGN structure.

1.1.2 UNIFICATION

The unification model describes all types of AGN in one model by showing how we can explain them through just their basic properties, as their emission processes and geometry otherwise essentially remain the same. The main thing that changes is the way in which we are viewing the AGN (Ehler et al., 2018). This unification model is shown in Figure 1.3, and it includes the different classifications that depend on our viewing angle.

Blazars are a classification that applies to quasars, which are highly luminous AGN that also produce jets. The blazar classification is for when the AGN is viewed

face-on, such that we are directly viewing the central engine and, thus, are in the direct path of the jet (Blandford et al., 2018).

Seyfert galaxies are low-luminosity counterparts to quasars and are the most common AGN in the local universe. The sub-classification of these galaxies depends on our line-of-sight in relation to the obscuring torus. In this classification, the emission we see is different as this viewing angle is changed. Seyfert I galaxies are galaxies at which the inclination is generally close to face-on, meaning that there is no component of the torus that is obscuring our view of the emission. These types are ideal for trying to understand the processes that occur in this central region. Seyfert II galaxies are then those galaxies that are highly obscured mainly due to the dusty torus component being directly in our line-of-sight. There are additional types of Seyfert classifications between I and II, with their numbers being determined simply by how much of the AGN then becomes obscured by components such as the dusty torus. Between 1 and 2, there are what we classify as intermediate type Seyfert galaxies (such as 1.2, 1.5, 1.8), which effectively mix the aspects of the other two, such as having in-between viewing angles. The central engine is then most easily studied using Seyfert 1 galaxies, as they are the least obscured (Ehler et al., 2018).
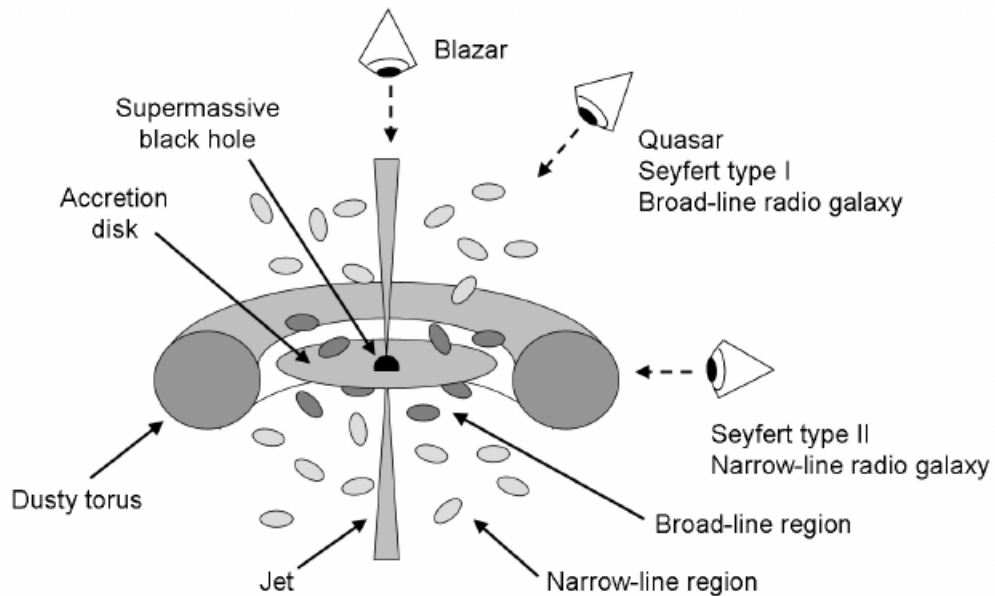
Figure 1.3: An illustration showing the unification model for an AGN. Various viewing angles are included to show how blazars and Seyfert galaxies are classified. Taken from Zackrisson, 2005.

1.2 THE X-RAY EMITTING REGION

1.2.1 VIEW OF THE SPECTRUM

Using detectors on X-ray telescopes, we can detect X-ray photons from these various sources. These detectors measure the photon arrival time and energy, which we use to then construct spectra and light curves that show changes in brightness as a function of energy or time, respectively. This information can give indications of emission of various materials (mainly through emission lines) and absorption through various materials (mainly through absorption lines and absorption edges). We can generally notice emission lines as narrow sharp increases in flux, while the absorption lines will appear as narrow sharp decreases in flux, and absorption edges as sharp discontinuous

drops in flux. These absorption edges occur when the electron in the ground state is ionized. Absorption edges are usually accompanied by an emission line as another electron de-excites to fill the ground state.
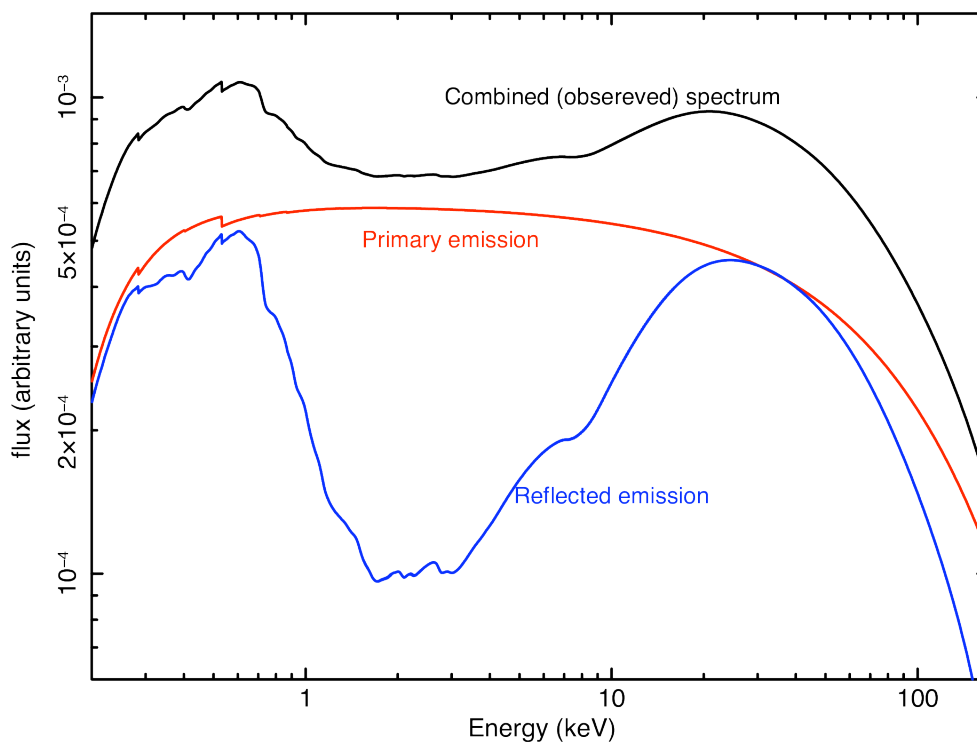
Figure 1.4: Plot of AGN spectra from 0.3 to 100 keV. It shows both the primary and reflected emission components, along with the observed spectrum that is the sum of the two. Taken from Gallo, 2011.

In our AGN spectra, we tend to concern ourselves with mainly one emission line in particular, which is the Fe Kα line that is around 6.4 keV. This line tends to be quite prominent, which is a result of iron being very prone to fluorescence, thus, making emission connected to Fe quite noticeable in spectra. Since this line is also not really close to many other lines in the spectrum, it is often well distinguished, even through
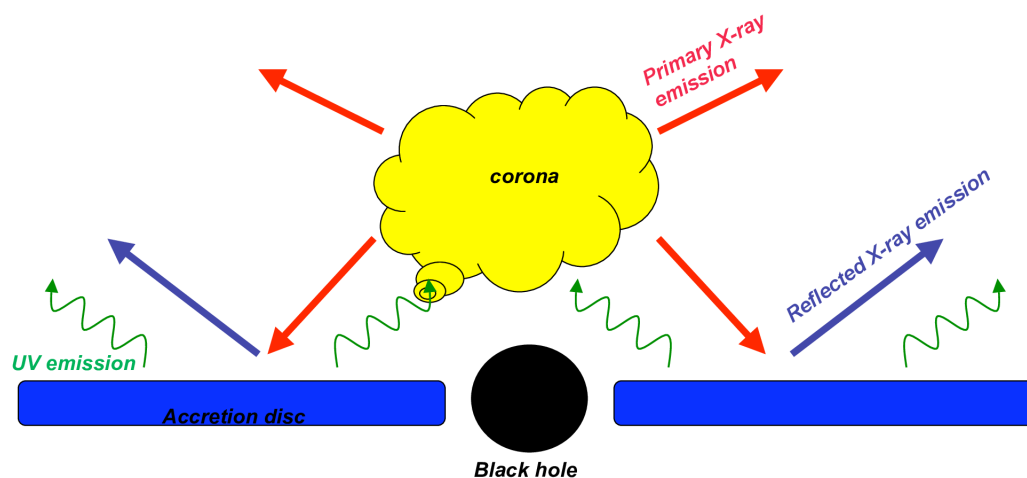
Figure 1.5: Illustration of how the primary and reflection emission components are generated within the central region of AGN. Take from Gallo, 2011.

relativistic effects, gravitational blurring and Doppler shifting that otherwise may alter its appearance or blend it with other spectral features (Gallo, 2011). General X-ray spectra consist of two components, which are a primary emission component and a secondary component that consists of reflected emission. The spectra we then see ends up being the sum of both of these components, as shown in Figure 1.4 (Gallo, 2011). A physical depiction of these components is shown in Figure 1.5 and will be elaborated on in the next two subsections.

1.2.2 PRIMARY X-RAY SOURCE

The primary source of X-rays in AGN spectra comes from the hot electron corona. As seed UV photons are emitted from the accretion disc, some portion of them will interact with the corona where they will undergo a process called Comptonization. This process involves the scattering of these UV photons to higher energies by the coronal electrons as they impart some energy on the photons. These photons are then released isotropically from the corona as X-ray photons. The emission we see from this primary component occurs in the form of a power law with a cut-off at a high energy (generally taken to be around 300 keV), which can be used to discern the temperature of the corona (Gallo, 2011).

1.2.3 REFLECTED COMPONENT

The secondary component of the spectrum is reflected emission. It is a result of high energy X-rays colliding with the cooler accretion disc and ionizing heavier atoms. Through processes of absorption and emission, a line-rich spectrum is created. The spectrum is then blurred for the gravitational effects given its proximity to the black hole (Gallo et al., 2011). Most of these high energy X-ray photons are from the primary emission component and, thus, come from the corona. Since the corona radiates isotropically (equally in all directions), some of the photons reach the accretion disk and ionize the ground-state electrons. The surrounding electrons cascade to lower energy levels emitting photons in a process called fluorescence. Thus, emission lines from the reflected spectrum can give insight into various properties of the accretion

disc, including insight to the various important processes occurring in this region (Gallo, 2011).

Narrow emission lines, such as the iron emission line, are highly affected by the AGN environment. These lines can be subject to three different effects, which are Doppler broadening, special relativistic broadening, and general relativistic broadening. Since the accretion disk is constantly revolving, from the perspective of an observer, some radiation will appear to be moving away (redshifting) or will appear to be moving towards them (blueshifting). This results in a portion of the emission line being shifted to bluer (higher) energies and another portion being shifted to redder (lower) energies, which results in a double-peaked profile for that emission line.

Now, if we go closer to the black hole to the point where material can move at significant fractions of the speed of light, the emission line will undergo special relativistic broadening. This effect occurs due to beaming, where light moving towards us at these speeds will appear much brighter, while the light moving away from us will be dimmed. This is analogous to a ship viewing the light from a lighthouse, where the light from the lighthouse will appear much brighter when shining towards the ship but will appear significantly dimmed when pointing away from the ship. In the spectrum, the emission line will now be asymmetric, as the special relativistic broadening causes a shift of the emission line to redder energies.

Moving even closer to the black hole, there is a significant gravitational potential well that can lead to general relativistic broadening of the line. In order to escape this well, photons trapped within it will have to expend a significant amount of the energy

and, thus, photons making up the emission lines that have escaped from this well will

appear to be at significantly redder energies. This effect only increases as photons

come from increasingly closer to the black hole. Thus, general relativistic broadening

results in the emission line being stretched to redder energies. The emission line

profile then involves the combination of all these effects as seen in Figure 1.6 (Gallo,

2011).
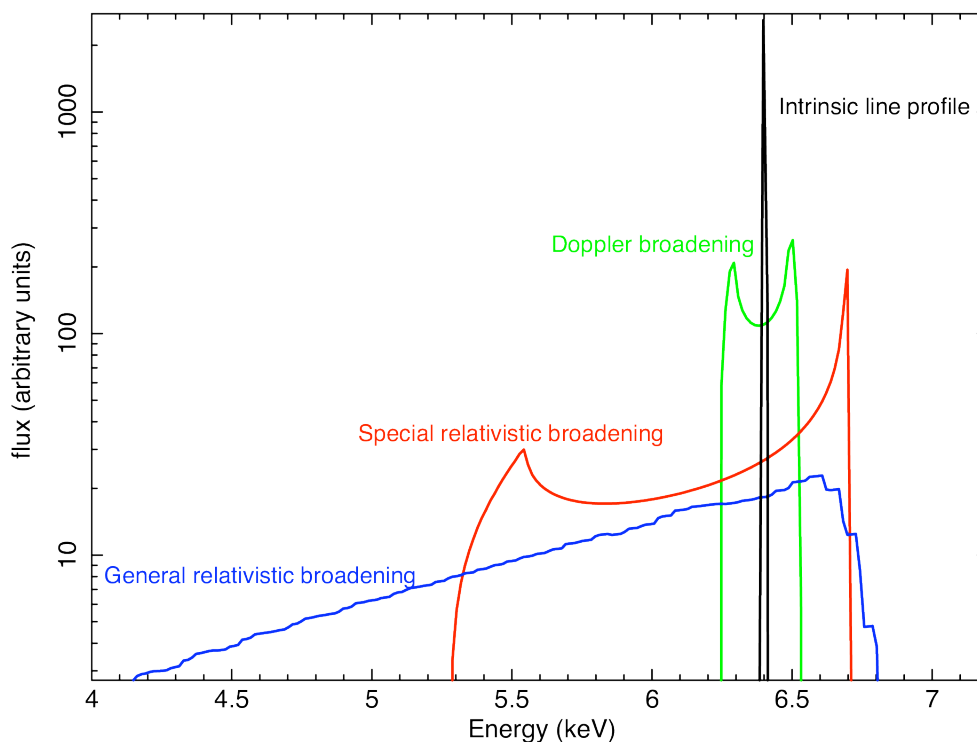
Figure 1.6: Spectra plot showing the effects of the AGN environment on narrow emission lines. Three effects are shown: Doppler broadening (green), special relativistic broadening (red), and general relativistic broadening (blue). Taken from Gallo, 2011.

Usually, the primary component is the dominant component in the spectrum.

This would make sense as the primary component is what ultimately leads to the

reflected emission, and the isotropic nature of the primary emission means that many photons do not interact with the accretion disk, thus, causing less to be detected from the reflection component. On occasions, the reflection spectrum has been seen to be the dominant component, and that would require that something must be diminishing the primary emission but would have a somewhat negligible effect on the reflected emission. This is explained through the concept of light-bending, where the gravitational influence of the SMBH causes the paths of many of the emitted photons to curve back towards the black hole. As a result of this, less photons escape the region and reach our detectors, thus, the primary emission will appear quite diminished. It only happens if the corona (the source of primary emission) is close enough to the SMBH because the gravitational pull would be too much for many of the primary photons to overcome. With more light being bent inwards, this means that more photons will be in the inner region of the AGN, increasing the likelihood that photons could interact with the accretion disk and then be reflected off of it. Light bending can both diminish the primary emission and augment the reflected emission, causing some cases where the spectrum appears to be reflection-dominated (Gallo, 2011).

1.2.4 SOFT EXCESS

Generally AGN spectra are well-fit by a power law model, in an intermediate X-ray energy range like 2-10 keV. If extrapolated to lower energies, like 0.3-2 keV, the power law model fails to fit that data well, revealing a component called the soft excess. The

soft excess is probably the most uncertain component in AGN spectra, as its origin is not well known, but luckily this is a very active area of X-ray astronomy. As explanations for the soft excess, the two widely considered models are blurred ionized reflection or an optically thick plasma that causes significant thermal Comptonization of seed photons (Petrucci et al., 2018). Figure 1.7 shows how the power law model fails to fit an AGN (Mrk 335 in this case) in the lower energy range, thus, producing the shape of a soft excess. The feature will be further discussed in Section 1.2.6.
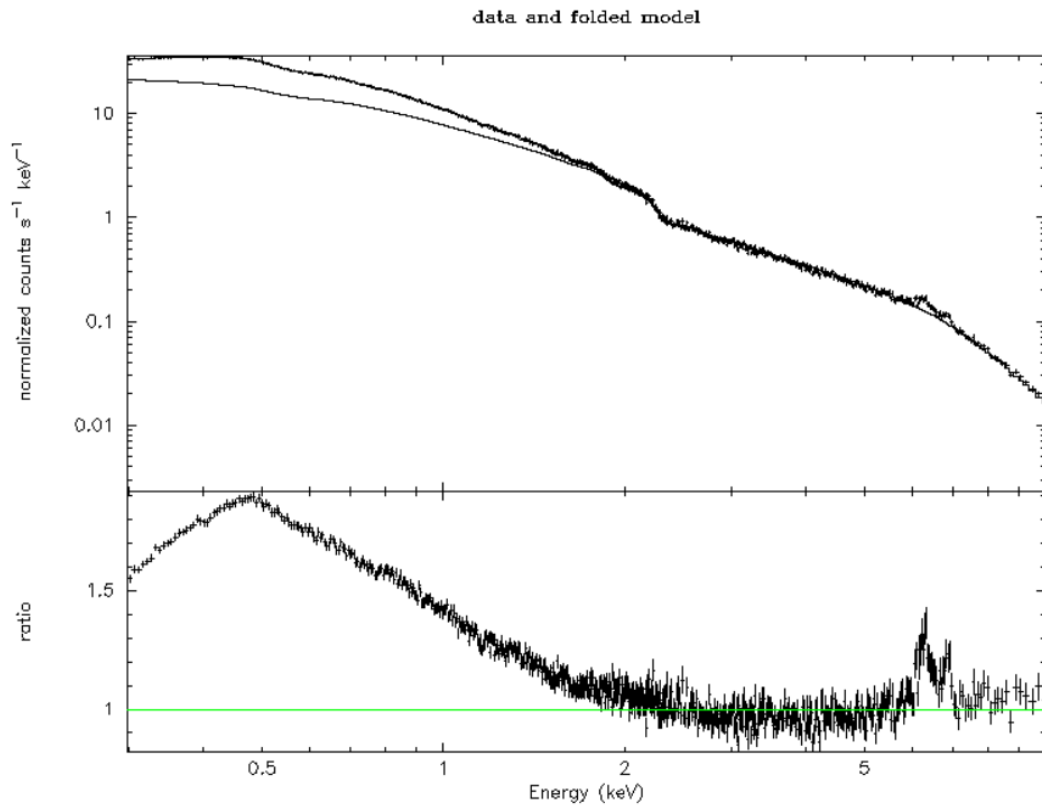
Figure 1.7: Spectrum generated in *xspec* for the AGN Mrk 335. It is fit with a power law (Γ=2) from 2-10 keV and then extrapolated down to lower energies (0.3-2 keV). The lack of a good fit below 2 keV, as seen in the residuals (bottom) indicates the presence of the soft excess component. The presence of the Fe Kα line at around 6.4 keV is also noticeable.

1.2.5 COMPTON HUMP

The Compton hump is a component at higher energies (generally between 10-80 keV), that is effectively a hard excess, a high-energy analogy to the soft excess. In this energy range, there is a large occurrence of Compton down scattering, which results in an excess of photons being moved up to this energy range, thus, providing a component at high energies that is not well-fit by a power law model. This component, however, is not shrouded in as much mystery as the soft excess and is a predicted feature for the reflection process (Kara et al., 2015).

1.2.6 GENERAL MODELS

The general models we talk about when it comes to AGN are used to help explain the various features we observe in spectra but are particularly used to understand the driving physics and analyze parameters. These models that we consider alongside the reflection component, in order to help explain things like the soft excess, are soft Comptonization and partial covering models, along with some blurred reflection.

Partial covering models consider an obscuring gas that only partially covers the emitting source. This results in the absorber covering some percentage, referred to as the covering fraction (f_c), of the emitted X-rays, where 1-f_c percent of the X-rays reach the observer (Grinberg et al., 2020). Studies have shown that a lot of absorption variability is due to changes in covering fraction, generally meaning that changes in absorber geometry could result in the extreme variability we see. AGN spectra that have a deep iron K-absorption edge and also show a lack of fluorescence are usually

best fit with this type of model (Tanaka et al., 2004). This is present in many AGN and, thus, the idea of continually changing partial covering absorbers can fit with absorption variability in most AGN.

The coverer can generally be thought of as an absorbing cloud of gas. This cloud would have "holes" in it (patchy), or in some other way, only absorb a fraction of the emission, even if it largely obscures along the line of sight (Tanaka et al., 2004). These absorbers are generally compact, dense and cold, and located close to the X-ray source. Since these absorbers are generally clouds/clumps of gas, they can be made up of various materials, so analyzing partial covering models can give information on the element make-up of the obscurer and can further be used for the determination of black hole mass through dynamical studies. The proximity to the X-ray source means the cloud is likely ionized (Grinberg et al., 2020). Some theories have been formulated that indicate that ionized partial covering could be a good explanation for the soft excess. It is possible that a soft excess can be manifested from absorbing intermediate energies on the power law (Tanaka et al., 2004).

Often considering a single partial coverer is enough, but double or even multiple partial coverers can be considered. Some studies have found that with multiple different partially covering absorbers, one can be neutral while others can be ionized, which gives indications/details about the cloud geometries. The consideration of two partial absorbers can be mainly one of two things, which are either having two different absorbing regions not connected to one another or simply gradual differences in column density along line-of-sight that impact the amount absorbed (Tanaka et al., 2004).

The blurred ionized reflection model considers reflection off of a region of ionized material that is then blurred due to relativistic effects as a result of the central black hole's gravitational influence. It is possible that this model can entirely take the place of the power law model and fit the data quite well. Generally, to be blurred, this reflection must occur close to the black hole, meaning that in this case it is likely to be reflection off of the inner accretion disk. Analyzing this reflection has allowed for some information to be gained on the make-up of these components. The neutral Fe Kα line and how narrow it is, indicates it originates in neutral distant matter. The Doppler broadening of the neutral line is small, indicating that it is definitely located somewhere outside of the broad line region and likely the torus (Fabian et al., 1989).

Reflection off of the inner accretion disc shows many of the lines being substantially broadened by the black hole gravitational influence, which indicates that this component is located much closer and likely at the inner accretion disc. This is then a good explanation for the soft excess as the broadening and blurring of lines in this area causes a large hump without any noticeable features, as the large amount of lines down in this range tend to be blurred in this way (Ehler, 2019).

Thermal Comptonization from an optically thick plasma involves a generally warm (kT = 1 keV) plasma upon which scattering (in the way of Comptonization) occurs. Warm Comptonization would produce photons with energies in the soft X-ray ranges. The two-corona model considers a warm corona producing the soft excess and the hot corona that produces the higher energy continuum emission. The location of this warm corona is likely to be around the inner region of the accretion disk. In this configuration, since the warm corona is not as hot as the other corona, it is likely to

impart less energy on the UV photons through the Comptonization process than the

hot corona, resulting in soft Comptonization (Petrucci et al., 2018). Figure 1.8 shows

a theoretical orientation for this two-corona model.
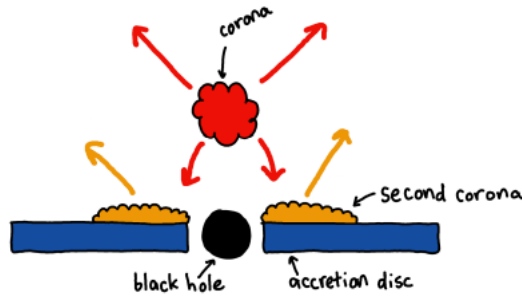
Figure 1.8: Depicted is a two-corona model, where the second, warm corona (orange) is located around the inner accretion disk. As is evident, some of the radiation from the primary, hot corona (red) interacts with the warm corona and is later emitted. Taken from Ehler, 2019.

1.2.7 SPECTRAL MODEL DEGENERACIES

Through spectral analysis of AGN, it is noticed that there are three models that fit

equally well in the 0.3-10.0 keV band. These degenerate models are partial covering,

Comptonization, and blurred reflection, as each of these along with a base power law

model can well explain both the 2-10 keV continuum emission and the soft excess

component (Ehler et al., 2018). This difficulty to distinguish models comes into play

when trying to determine the source of the soft excess.

The importance in distinguishing between these models is in giving a better un-

derstanding of AGN geometry. Narrowing down the model and parameter changes

that result in the observed variability then allow for further development of how com-

ponents interact within AGN. For example, certain changes in the partially covering

absorber (which we could see in things like varying ionization or covering fraction) would be useful for understanding what this absorber is and how it interacts with other components. With an appropriate model determined, we can then start to constrain other properties we are interested in, which could allow us to determine the abundance of elements like iron. Thus, we learn the most about AGN, or any X-ray source for that matter, when we are able to pinpoint all the processes occurring in the system.

1.3   HARDNESS RATIO (HR) ANALYSIS

In more recent times, a new idea for analyzing spectral variability has been developed and applied to studies of various X-ray sources. It involves analysis in colour-colour space, which itself is nothing new, but recent studies have employed comparisons of data to tracks on these diagrams as a way to characterize variability. These shapes are an essential part of HR analysis, as they are formed by the paths taken for different parameter changes in our models. Thus, getting real and/or simulated data and comparing to these tracks should help us determine the appropriate model and associated parameter variations.

HR analysis is useful for exploring X-ray variability especially in cases where detailed spectral analysis can often be impossible with current X-ray instruments. This is true when variability occurs on short timescales, such that observations cannot offer detailed information about the process. A successful application of this method was shown in Grinberg et al. (2020), so their method is important to consider here when it comes to trying to pinpoint the source of X-ray variability. In their case, they used this method to analyze variability in high mass X-ray binaries (HMXBs), where various processes can vary on short timescales making detailed spectral observations impossible.

In the case of HMXBs, we have a binary consisting of either a black hole or neutron star with a massive companion star that the compact object accretes from. This study deals with an O/B type companion with the compact object. There is a large amount of "clumps", which can generally consist of gas from the stellar wind, that are passing

across the line of sight of the observer. When studying X-ray absorption variability for HMXB systems like this, these clumps of gas are the source that is generally looked at. Thus, it makes sense that models including absorption and partial covering should be used for HR analysis. As this system can be at high temperatures and can be densely packed, it is important to consider the possibility of ionization, something that this study includes to improve on previous studies surrounding HMXB variability.

Grinberg et al. (2020) constructed grids, using Chandra HETGS/MEG responses, to model a partially absorbed power law model and considered parameter changes in covering fraction, column density, and photon index, while also considering different ionization types (neutral, warm, etc.). Then, using a Chandra observation of the HMXB, Cyg X-1, they constructed curves in colour-colour space that they compared to the Chandra colour-colour grids. As shown in their work, these types of studies have the potential for broad use on determining the source of absorption variability for different X-ray sources. Their study has shown that this method can be applied to high mass X-ray binaries (HMXBs) and yield useful results about the origin of the variability and the changes in parameters associated with this variability. Comparisons with some real data led to the conclusion of an ionized partially covering absorber being responsible for the variability. It showed that the best fit was a case where ionization was inversely dependent on column density, and they were also able to show that its ionization and covering fraction changing are likely the reason for the variability. Figure 1.9 shows an example of one of the colour-colour diagrams that they used during their analysis (Grinberg et al., 2020).

The problem they encountered is much the same as the reasoning for why this

method should be useful, in that they were trying to narrow down the source of X-ray variability even more by trying to further break through model degeneracies. After seeing their success in doing so, it shows that colour-colour grids can allow for a unique opportunity to assess spectral variability and to determine physical processes resulting in variability. This success is good motivation for exploring this method further and attempting to use it with AGN, especially as further success could result in wider applications of these grids across even more studies.
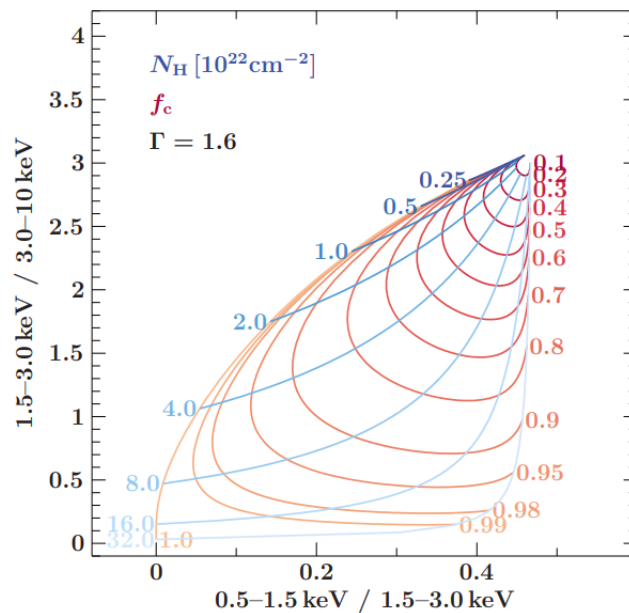
Figure 1.9: Shown is an example of a colour-colour diagram with two free (varying) parameters. The diagram, created with $\Gamma=1.6$, has f_c varying between 0.1 and 1.0 and N_H varying between 0.25 and 32.0 (in units of $10^{22}\ cm^{-2}$). Taken from Grinberg et al., 2020.

Other studies that motivate me to use colour-colour grids here are those by Carpano et al., (2005) and Nowak et al., (2010). In the former, they used these diagrams with the goal of determining the properties of point sources in the optical disk of NGC 300. Spectral modelling was not viable as it would only give enough

detail for really bright point sources. Through observations of the optical disk point sources, they were able to form a set of points in colour-colour space that they could check for properties. To set up their grids, they found the hardness ratios with a simple bremsstrahlung model and with a bremsstrahlung plus power law model, where the varied parameters were photon index, disk temperature, and column density. By comparing the set of points to these model grids in colour-colour space, they were able to determine which model well-described all but one of the point sources (Carpano et al., 2005).

In the latter study, they attempted to use colour-colour diagrams to model the dust scattering halo believed to be present with Cyg X-1. To describe this, they modelled it as an absorbed disk plus power law at different levels of absorption, with the varied parameter being the optical depth of this halo. Using data from a Suzaku-XIS 1 observation, they created a set of points in colour-colour space and compared it to the diagrams, which led to a suitable range of optical depth values for the halo. Afterwards, they analyzed their errors and determined that their data was not of the best quality and, thus, the colour-colour diagrams did not completely fit the properties of the halo, however, Grinberg et al., (2020) did improve on this as mentioned (Nowak et al., 2010). Based on the fact that, in both papers, they were able to discern some properties of various X-ray sources through using colour-colour diagrams, it is clear that these diagrams at least provide some use in analysis. Thus, all of this is perfect motivation for attempting to use colour-colour diagrams towards AGN variability.

1.4 THIS WORK

In this work, we set out to use colour-colour grids to distinguish between AGN model degeneracies and attempt to better pinpoint the source of emission and variability. We strive to determine whether blurred reflection, Comptonization, or partial covering is responsible for this variability in a given source. This can also provide us with the parameter variability that is occurring. We begin by using an XMM pn response file to construct colour-colour grids for different parameter combinations for each model. Three energy bands within the important 0.3-10.0 keV band are considered, and we denote them as Band 1, Band 2, and Band 3. One of the models is then "folded" through the response and model predicted count rates are extracted within each band for each combination of parameter values, as they are varied throughout the process. The normalization is ignored. While it impacts the count rates, the HRs are unaffected. From these, we determine hardness ratios (colours) by using the count rates and taking Band 1/Band 2 (soft colour) and Band 2/Band 3 (hard colour). We then construct our instrument-specific colour-colour grids by plotting hard vs. soft colour, noting the tracks carved out by various parameter changes, such as can be seen in Figure 1.1. Grids are then compared to both simulated data sets and real data from an observation of NGC 6814. These comparisons should provide information about the most fitting model for the data and the associated parameter variations. This can then inform our view on what is happening in the system physically to result in this variability. This will be elaborated in much more detail in the Experiment and Method section. As we have seen here, there is a lot we still do not know about

AGN, including much surrounding geometry of various AGN components. Therefore, it is through unique studies, like those done in Grinberg et al., (2020) that we can finally help shed some light on these unknowns.

Chapter 2

EXPERIMENT AND METHOD

2.1 XMM-NEWTON

All simulations and data used in this work are based on XMM-Newton, a telescope that is popular and widely used in X-ray astronomy. It is one of the most important X-ray space telescopes due to its wide range of applications in this field. Launched on December 10th, 1999 into a 48-hour orbit, the X-Ray Multi-Mirror Newton Observatory (XMM-Newton) set out to improve the state of X-ray missions at the time. Its main goal was later identified as trying to improve the state of X-ray observations of faint sources, thus, allowing for X-ray spectroscopic analysis that was of high quality (Jansen et al., 2001).

The main thing that makes this telescope preferable over other X-ray telescopes is that it has three mirrors each with a large effective area, and works over a broad energy bandpass. The telescope features the Wolter 1 design, consisting of 58 nested mirror shells that share the same foci (confocal) and are centered around the same central axis (coaxial). Of these mirrors, the largest have a 70 cm diameter and grazing incident angle of 42 arcminutes, and are the outermost ring of the mirrors. The innermost mirrors have a diameter of 30.6 cm and grazing incident angle of 17

arcminutes. This system of mirrors also has a focal length of 7.5 m and they are all covered in a gold reflective coating.

The main readout camera is the European Photon Imaging Camera (EPIC), which offers very useful X-ray imaging capabilities due to the sensitivity of the three CCD imaging cameras. There are two MOS (Metal Oxide Semi-conductor) CCDs (Jansen et al., 2001) and one pn CCD (Jansen et al., 2001). The pn is an arrangement of 12, 3 x 1 cm CCDs (Jansen et al., 2001). This portion of the telescope has high efficiency when it comes to photon detection (Jansen et al., 2001). For high resolution spectroscopy, there is the Reflection Grating Spectrometers (RGS) (den Herder et al., 2001). These are not used in this work. All of these components can be seen in Figure 2.1.
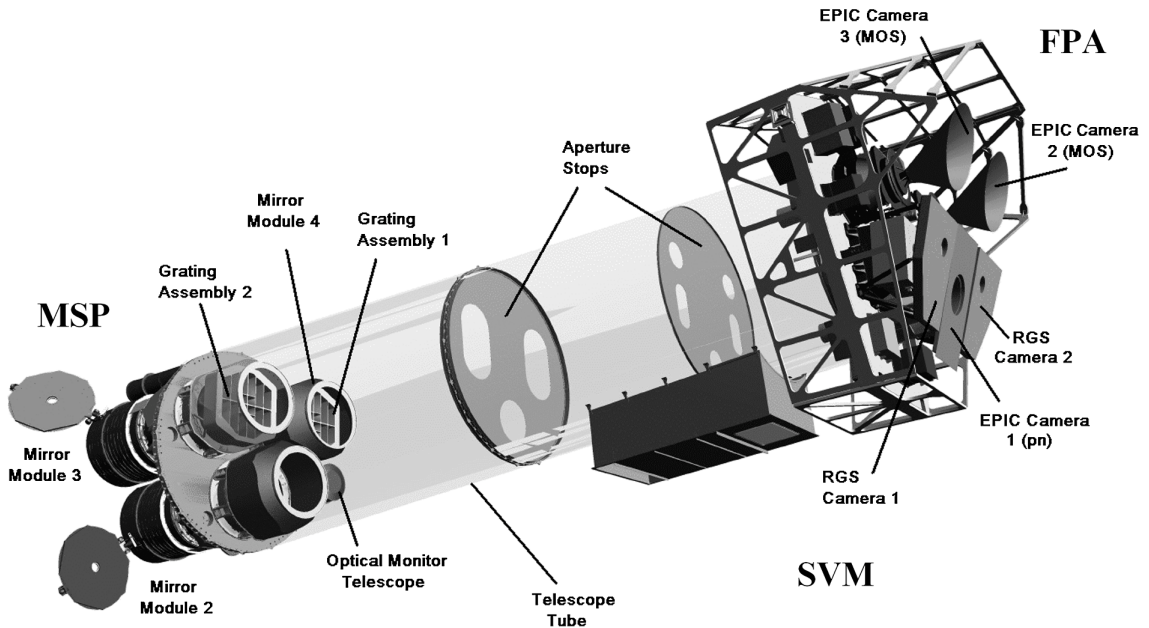

Figure 2.1: This diagram shows the general layout of XMM-Newton with the locations of various important instruments indicated; taken from Lumb et al. (2012).

2.2 CREATING COLOUR-COLOUR GRIDS

In optical astronomy, a colour is the difference between the brightness in two different filters (e.g. B-V and U-B). In X-ray astronomy, a colour is more often called a hardness ratio, which is the ratio in the count rate in two different energy bands. Since count rates depend on the energy-dependent response of the detector, colours are specific for each telescope-detector combination. Colours can net us useful properties of the system we are studying. In optical, colours tell us about stellar properties, like temperatures. For variable AGN, hardness ratios tell us about changes in spectral shape. Thus, for AGN, these can provide us with information about many different parameters, such as photon index and black hole mass.

The method adopted here was similar to that done in Grinberg et al. (2020). To generate a hardness ratio, the XMM-Newton EPIC-pn instrument response file was loaded into the X-ray Spectral Fitting Package, or *xspec*. A model could then be constructed within *xspec* and "folded" through the detector response. The brightness and appearance of the spectrum would be specific for the telescope.

Two colours were constructed based on the count rates in three energy bands: 0.3-1.0 keV (soft), 1.0-4.0 keV (mid), and 4.0-10.0 keV (hard), with the soft colour taken as soft/mid and the hard colour taken as mid/hard. These bands were chosen to represent three distinct regions in the AGN spectrum (Fig. 1.4 and 1.7). The soft band is chosen to be 0.3-1.0 keV, where the soft excess exists. Figure 1.7 shows that the soft excess component is contained around this energy range. Since this component is an important part of the spectrum when it comes to determining appropriate

models, and it is still not well explained for many AGN, there is a need to isolate it in our colours. To represent the continuum emission (i.e., the portion best described by a power law) well, the 1.0-4.0 keV is chosen as the mid band, as the power law model has been found to work well in this range. The hard band is chosen to be in the range of 4.0-10.0 keV to represent the harder portion of the AGN spectrum, a portion that contains the Compton hump component.

For a given model, up to two parameters are varied independently within a defined range, with all other parameters remaining frozen to avoid confusion. Model count rates are extracted from the predetermined energy bands, and recorded. To generate the grids themselves, the colours are calculated and plotted using Python code. This led to the construction of seven grids based on three AGN interpretations. One for an absorbed power law (Comptonization), three for partial covering (absorption), and three for relativistic blurred reflection (Section 1.2.6).

2.2.1 POWER LAW

The power law model is useful for describing the primary emission in AGN. This model is characterized by its photon index Γ, which is typically in the range of $\Gamma=1.5$ to $\Gamma=2.5$. Photon index has been found to be almost directly linked to accretion rate, and further studies have indicated a positive correlation between photon index and X-ray luminosity (Yang et al., 2015). Thus, flux detected in our spectra, due to primary emission, should be expected to increase as photon index increases.

This model was the first one constructed and "folded" through the response,

where count rates were extracted from each energy band for values between Γ=1.0

and Γ=3.0 in steps of 0.2. By plotting the resultant colours, we generate a track

for this parameter variation. This track can be seen in Figure 2.2. In this simple

diagram, it is noticed that both colours are increasing as photon index increases. It

appears as if the track follows an exponential shape, as difference between successive

points seems to be changing at such a rate. This simple exercise already generates

a result. If the photon index of an AGN were changing over time, then we would

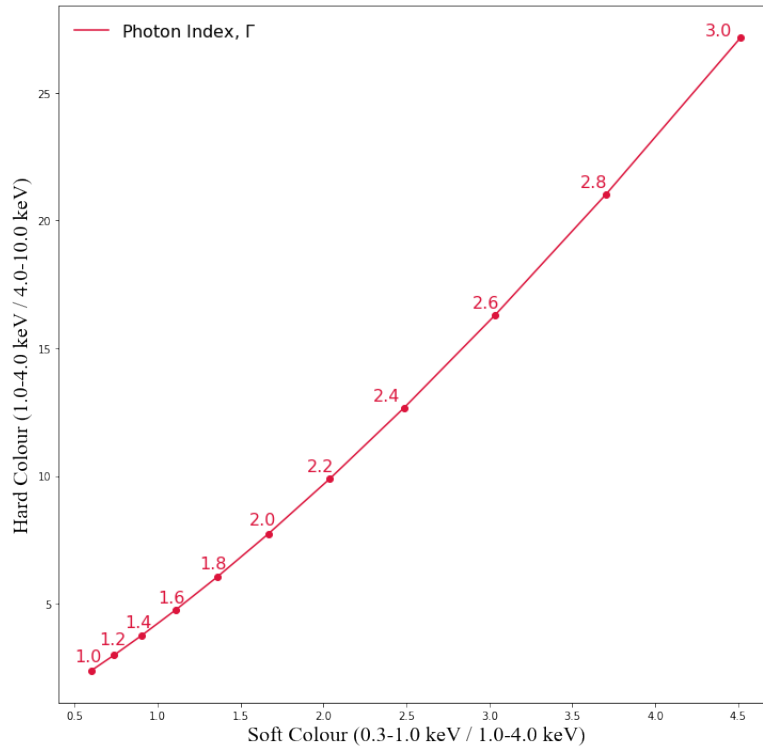expect its colour-colour diagram to resemble this trend when plotted.

Figure 2.2: Colour-colour track for varying photon index in pure power law model, using XMM pn response. The values on the curve are for the photon index that produces the corresponding colour.

2.2.2 ABSORBED POWER LAW

Interstellar space contains gas and dust, commonly referred to as interstellar matter (ISM). The space between stars in galaxies consist of a lot of this ISM, with the gases primarily consisting of hydrogen, along with helium, and traces of carbon, nitrogen, and oxygen. As photons are emitted by different objects, such as AGN, they will interact with the ISM, transferring some of their energy to these materials. This absorption along our line-of-sight leads to photons reaching our detectors attenuated and possibly with lower energies (i.e. redder) than what they were emitted with. The amount of this matter along our line-of-sight is quantified by the Galactic column density N_H, which is often close to something on the order of 10^{21} cm^{-2}. Based on this, it would be expected that higher N_H would lead to lower flux and, thus, both soft and hard colours would be expected to decrease. However, since the absorption and scattering is wavelength dependent, one might expect the softer count rate to be affected more.

In our *xspec* models, the column density (N_H) is taken into account using the "tbabs" component. To account for the effects of this absorption on the power law ("po") spectra, we use the combination "tbabs*po" in *xspec*. For this situation, there are only two parameters seen to vary on observable timescales, which are Γ and N_H. With this in mind, we fold this model through the XMM response file and extract the count rates in each energy band for variations in both of these parameters. The photon index is varied just as it was with the power law grid, and the column density is varied such that the values are evenly-log-spaced, leading to fifteen values in the range

of 0.01 to 10.0, in units of 10^{22} cm^{-2}. The resultant colours are plotted accordingly to create Grid 1, as shown in Figure 2.3.

Expected trends are noticed from the parameter tracks in this grid. At low absorption, and high photon index, large values are seen in both colours, following the same expected trend as with the pure power law. The effects of increasing absorption are to lower the colour in both bands, as would be expected since this absorption reduces the number of soft photons reaching the detector compared to hard photons. At higher absorption, it can be noticed that increasing photon index has a negligible effect on the soft colour, but a significant effect on the hard colour. Since the power law is generally seen to be best fit for the continuum and harder portion of the spectrum, this trend would be expected. The Galactic column density in the Milky Way is not expected to change over the course of our observations. Such a model can be used to replicate the expectation of variable neutral absorption that is associated with the AGN or its host galaxy.
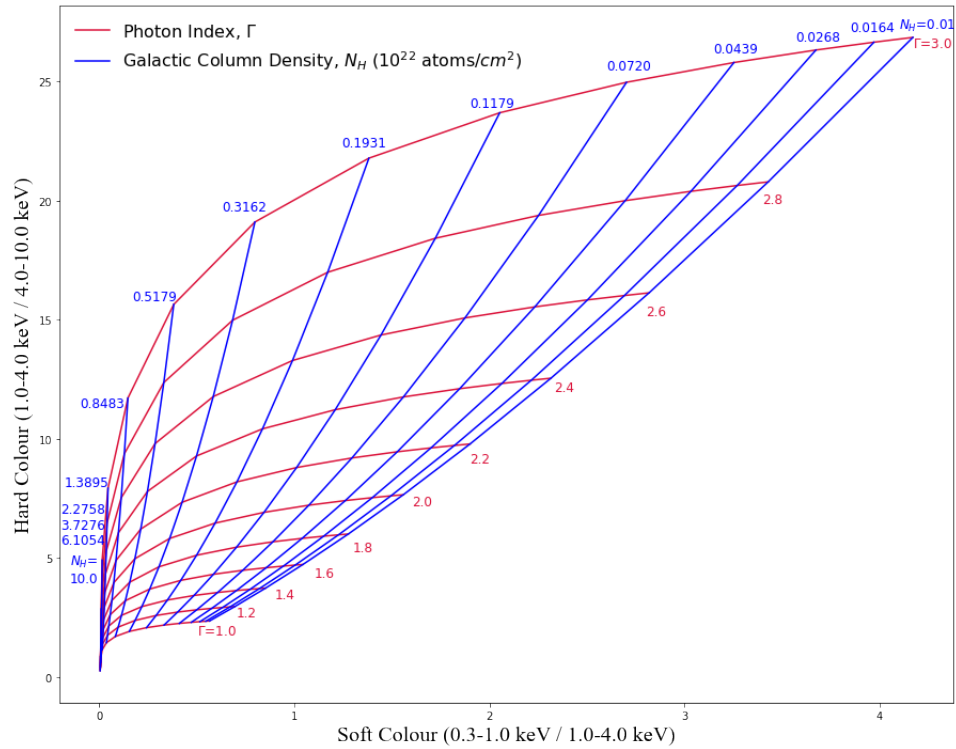
Figure 2.3: Grid 1 - Colour-colour grid generated for an absorbed power law model with varying photon index and galactic column density.

2.2.3 Partial Covering

With AGN, there are often clouds of materials that can cover portions of the light emitted from the source. These are generally referred to as partially covering absorbers and can have many different properties. They are generally described by three parameters that all can vary on observable timescales. The three parameters are the covering fraction f_c for the absorber over the source, the absorber column density N_H along the line-of-sight, and the ionization of the absorber, $\log(\xi)$. As the covering fraction increases, more of the source is covered and less of the primary power emission is seen. It would be expected that a higher covering fraction should lower the flux we detect predominately at lower energies, thus changing the colours.

There is an expected relation between the column density and ionization of the absorber based on the idea of self-shielding, leading to the trend of lower ionization with higher column density. This has been shown in Grinberg et al. (2020), where it is thought that, with a higher N_H, more of the atoms inwards are protected by the outer atoms, leading to a self-shielding process that protects the inner atoms from ionizing radiation, thus, decreasing the ionization of the absorber.

To account for this partial covering absorber, the "zxipcf" component was used. This was employed in the form "zxipcf*po" to determine its effect on the power law spectra. This model also takes into account the redshift of the source, which is a measure of how fast the object is moving away from us, although it was set to zero for this work. It also takes the photon index into account, but we leave it frozen to Γ=2.0, as we want to analyze the properties of the coverers and their effect on emission.

We then fold the model through the XMM response, extracting count rates for the different parameter variations through each of the three bands. Since the covering fraction is a percentage, it is varied between values in the range of 0.0 to 1.0 generally in steps of 0.1, but values of 0.95, 0.98, and 0.99 were also included. Absorber column density is once again evenly-log-spaced, however, it is now varied between values in the range of 0.1 to 10.0, in units of 10^{22} cm^{-2}. To account for both low and high ionization states, the ionization is varied between nearly the entire available range, from log(ξ)=-2.0 to log(ξ)=3.0 in steps of 0.5. In order to properly identify parameter tracks, three grids are generated to include variations of two parameters at a time. When not varying, covering fraction was frozen to f_c=1.0, ionization was frozen to

$\log(\xi)$=1.0, and column density was frozen to N_H=1.0 (in units of 10^{22} cm^{-2}. These

variations can be seen in Figure 2.4 (Grid 2), Figure 2.5 (Grid 3), and Figure 2.6

(Grid 4).

In varying N_H and $\log(\xi)$ for Grid 2, we can see many grid lines intertwining,

with some combinations becoming difficult to distinguish from others. It can be seen

overall, and especially at lower ionization values, that both colours are decreasing,

which is the expected trend for higher absorption. At higher ionization, where there

is expected to be less absorption due to the self-shielding idea, it would be expected

that there is some lack of decreasing colour, however, that is only noticed on this

grid for the soft colour. Increasing ionization will first increase the soft colour and

then the hard colour, especially at the higher absorption values. For ionization, this

is somewhat close to expectations based on the self-shielding. At lower absorption, it

is once again noticeable that it has a more significant effect on the soft colour. These

observations are interesting and indicates that partial covering has a stronger effect

at the softer end of spectra.

Grid 3 shows the expected trends for varying both N_H and f_c. As absorption

decreases, the colour increases in both bands, indicating that the flux we detect would

also be higher, as the photons would be absorbed by less intervening material. Much

the same occurs for f_c, where lower values (i.e., less of the source being covered) lead

to increases in both colours. With less of the source being covered, a larger percentage

of the emission is now able to reach our detectors, leading to these higher colours.

Grid 4 showcases a "fold" in the grid when parameter variations are occurring.

The same trend as before with the covering fraction is noticed once again in this grid,

and seems to be consistent at all ionization values. Increasing ionization is also found

to, once again, increase the colours in both bands, although there is a point where

it actually seems to lower the hard colour slightly. Regardless, the end points follow

the expected trends, with high ionization and low covering fraction leading to the

highest colours, and low ionization and high covering fraction leading to the lowest

colours. The trends for each grid, fit with what was found for the grids in Grinberg

et al. (2020).

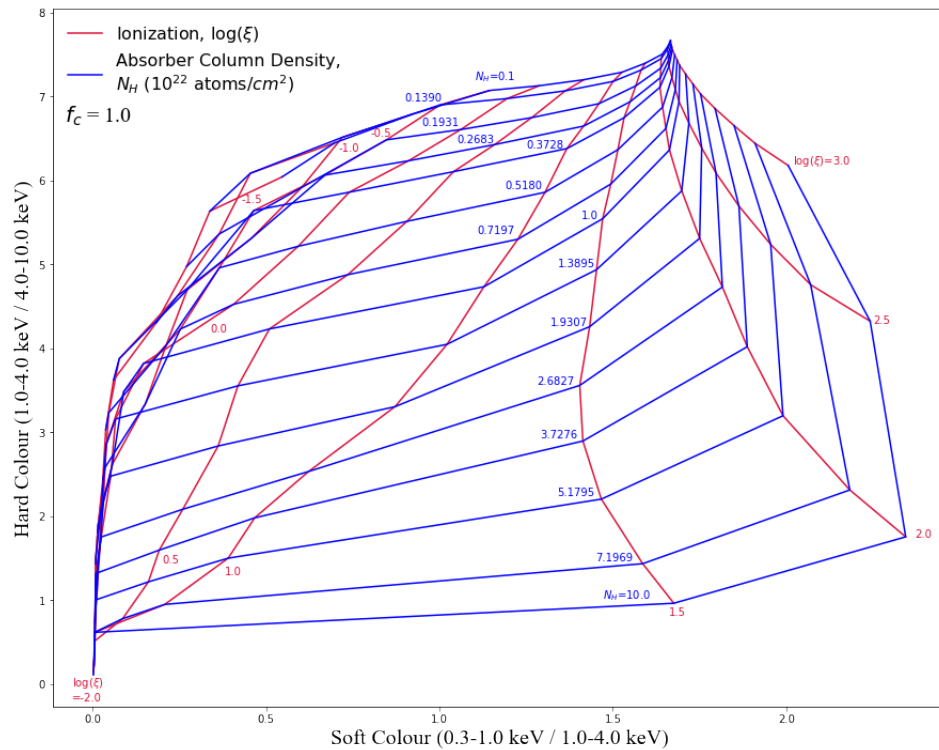Figure 2.4: Grid 2 - Colour-colour grid generated for a partial covering model with
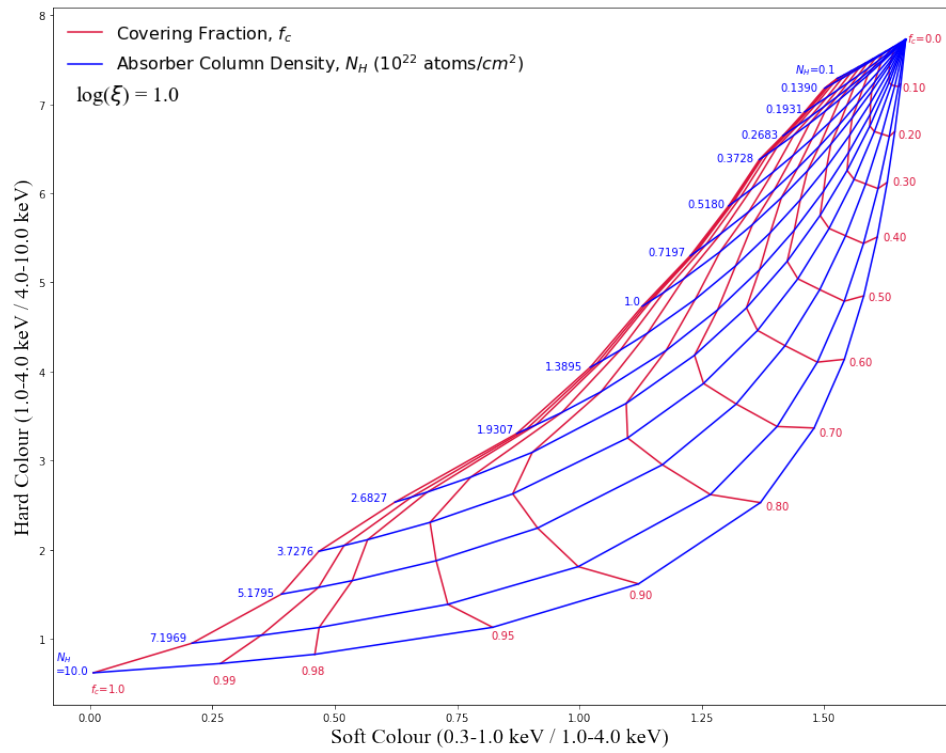varying ionization and absorber column density.

Figure 2.5: Grid 3 - Colour-colour grid generated for a partial covering model with varying covering fraction and absorber column density.
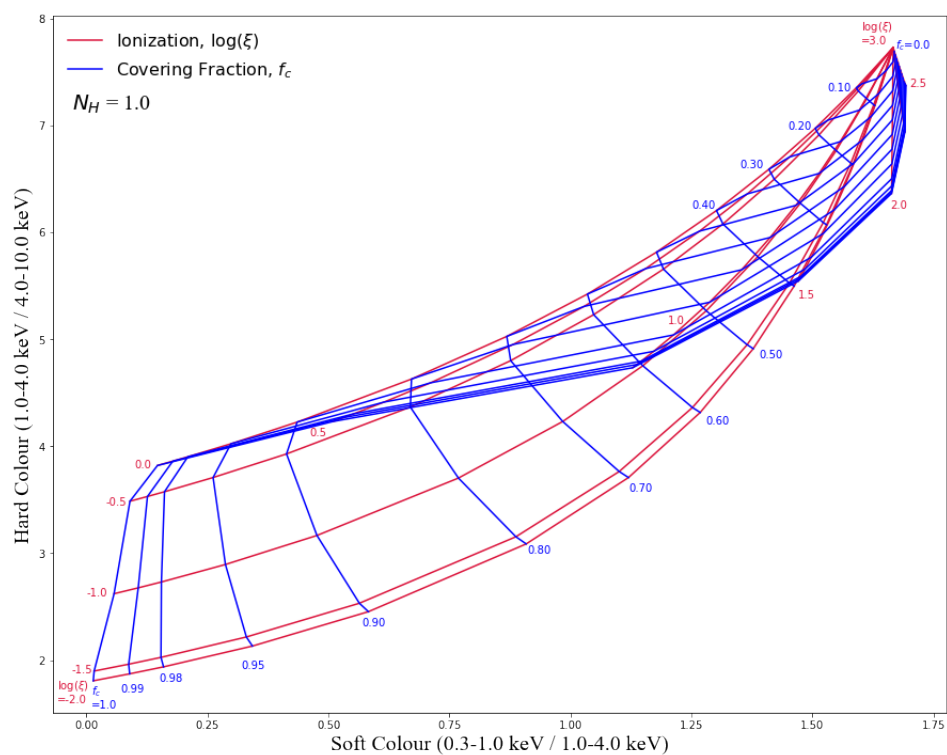
Figure 2.6: Grid 4 - Colour-colour grid generated for a partial covering model with varying ionization and covering fraction.

2.2.4 RELATIVISTIC BLURRED REFLECTION

As there is a prominent reflection component in AGN spectra, it is useful to consider the effects of this reflection off of the accretion disk for the HR analysis. The disk has various different properties that determine the significance of the relativistic blurred reflection off of the disk. Since the reflected flux depends on the primary emission, the photon index for the incident spectrum is an important parameter with this model. This reflection is defined by three parameters that are all expected to vary on observable timescales. These three parameters are the photon index Γ for the underlying power law, the ionization, $\log(\xi)$, of the disk, and the reflection fraction. The reflection fraction (R_f) is the ratio of the reflection-to-continuum emission during the observation.

To account for this, the "relxill" component was used, which is a standard relativistic reflection model in *xspec*. Along with the three indicated varying parameters, this model takes into account a slew of other parameters. These parameters are the spin parameter a_*, inner and outer radii of the disc (R_{in} and R_{out}), iron abundance, A_{Fe}, inclination of the disc i, inner and outer emissivity indices (q_{in} and q_{out}), redshift z, high-energy cutoff E_{cut}, and break radius R_{br} (Dong et al., 2020). The spin parameter characterizes the rotation of the central black hole by quantifying its angular momentum. A maximal spin parameter has a value of a_*=0.998, a value fitting for most AGN observed. Both R_{in} and R_{out} are the inner and outer radii for the accretion disk, respectively; a negative value gives it in terms of the innermost stable circular orbit (ISCO). For our purposes, we use R_{in}=-1, which places the inner portion at

the ISCO, and R_{out}=400, which puts the outer radius of the disk at 400 r_g, where

r_g=GM_{BH}/c^2. The iron abundance, which quantifies the amount of iron in the disk,

is frozen to A_{Fe}=1, giving it the same abundance as the solar abundance. Inclination,

which is measured as the angle towards the system measured from a line normal to

the accretion disk, is frozen to i=30°. We assume no redshift in these grids and, thus,

constrain it to z=0.0. For the reflection, its emissivity profile ϵ(r), is generally de-

scribed with ϵ(r) $\propto r^{-q}$, where q is the emissivity index and r is generally the breaking

radius. We set q=q_{in}, in the inner disk ($r_{in} \leq$ r $\leq r_{br}$), and q=q_{out}, in the outer disk

($r_{br} \leq$ r $\leq r_{out}$) (Dong et al., 2020). These are frozen to values of q_{in}=6.0, q_{out}=3.0,

and r_{br}=6.0 r_g. Finally, we have the high-energy cutoff frozen to E_{cut}=300 keV.

We then fold this model through the XMM response and extract the count rates

in each energy band for each variation in parameters. The photon index values are

varied in the same way as with the power law models. For the ionization of the disk,

we choose to vary it between log(ξ)=0.0 and log(ξ)=3.0 in steps of 0.2, with these

values being different than before, as "relxill" model only has a minimum ionization of

around log(ξ)=0.0. The reflection fraction is made to vary between values of R_f=0.0

to R_f=5.0. To properly identify parameter tracks, three grids are generated to include

variations of two parameters at a time. The resultant grids from plotting the colours

can be seen in Figure 2.7 (Grid 5), Figure 2.8 (Grid 6), and Figure 2.9 (Grid 7).

Looking at Grid 5, we see a sheet-like shape (Figure 2.7). The grid shows that

increasing photon index leads to an increase in both hard colour and soft colour,

which occurs for both high and low reflection values, and is consistent with what is

expected and what was seen for the power law grid (Figure 2.2). Increasing reflection

fraction is seen to cause increases in soft colour, but decreases in hard colour. The reflection component is said to be a likely source for the soft excess in many AGN and, thus, it makes sense that an increase in reflection would lead to a higher soft colour. Since more reflection is occurring, there are more photons that are then losing energy through this reflection process. This means that it is likely for there to be less hard photons and more soft photons, as many of the hard photons would be losing energy, resulting in the downward diagonal track we see for increasing R_f. At lower Γ values, it is noticed that the soft colour can start to decrease ever so slightly, but this is likely due to the effects of lower Γ, as explained earlier (Section 2.2.1). Earlier, the reasoning for increase in colours due to increase in photon index in this range was explained, and it follows that we see that trend here.

Grid 6 (Figure 2.8) appears to be a little more dynamic in shape than the previous grid. The increase in ionization at the smaller values causes a strong increase in soft colour, while at much higher values it causes a strong increase in hard colour. Overall, both colours increase. This is consistent with the increasing ionization in the partial covering models where we would expect a lower column density and, hence, less absorption, leading to a lack of diminishing flux in both bands (Section 2.2.3). However, at the lowest reflection fraction, the changes in ionization seem to have no effect on the colours. This is an indication that the ionization of the disk could be quite impactful on constraining the shapes of these grids. At low ionization, increasing reflection fraction can be seen to cause a decrease in both soft colour and hard colour, with the change in hard colour being much more significant. As ionization increases, this then transitions to a less significant decrease in soft colour until it eventually

starts to rise. However, the hard colour decrease is constantly present. Thus, we can generally see that increasing reflection fraction seems to have a decreasing effect on the hard colour, which is consistent with what was seen in Grid 5 (Figure 2.7).

Now, looking at Grid 7 (Figure 2.9), we can see some more interesting trends. As photon index increases, we once again see that both the soft and hard colour rise, which is consistent with what has been seen in other grids. When ionization is increasing, soft colour is seen to be significantly increasing, while there are only slight increases in the hard colour, with the tracks sometimes curving slightly backwards. The observation of increasing ionization having a significant effect on increasing soft colour fits with what we have seen already. Thus, these grids have shown that they are both consistent with each other and with the trends we would expect to see.
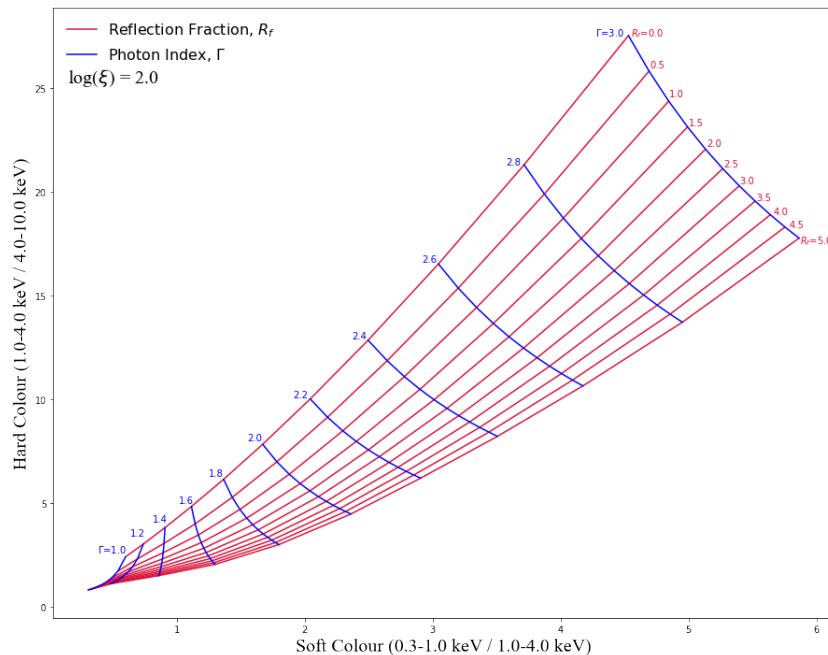

Figure 2.7: Grid 5 - Colour-colour grid generated for a relativistic blurred reflection model with varying reflection fraction and photon index.
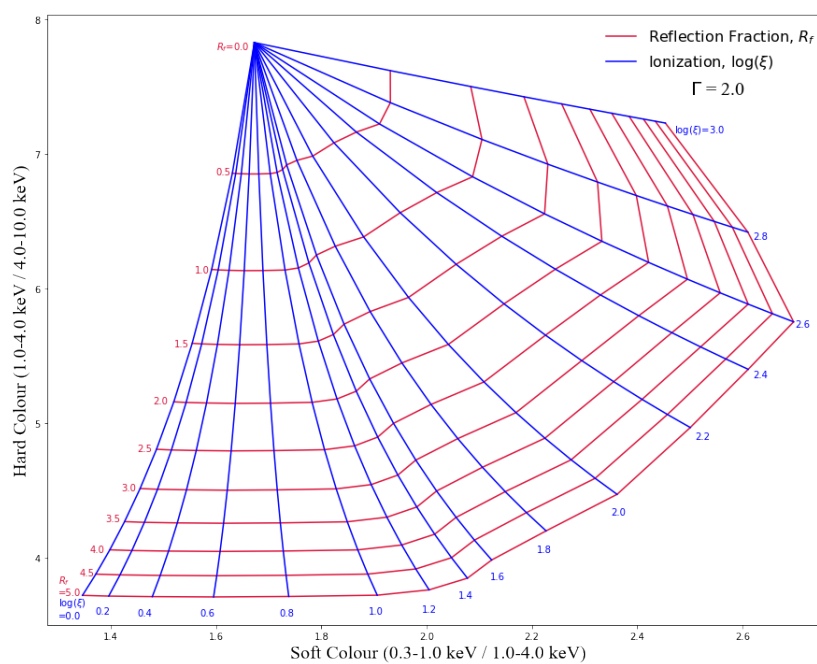
Figure 2.8: Grid 6 - Colour-colour grid generated for a relativistic blurred reflection model with varying reflection fraction and ionization.
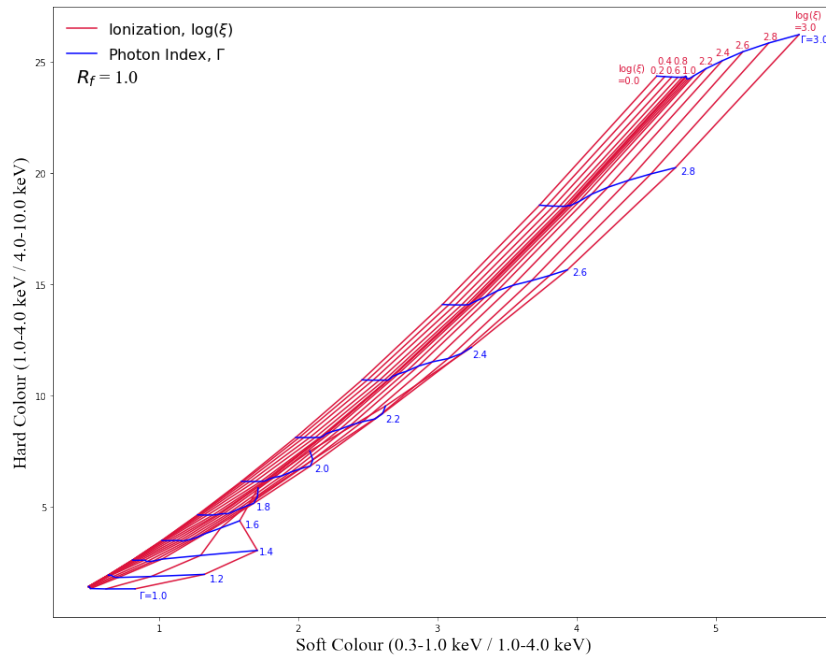
Figure 2.9: Grid 7 - Colour-colour grid generated for a relativistic blurred reflection model with varying ionization and photon index.

2.2.5 ADDITIONAL DIAGRAMS

Additional diagrams were tested to see if the results could be improved upon. One test was to consider the normalized hardness ratio so we could quantify the amplitude of the colour change compared to the total brightness. This involved defining the soft colour as (mid-soft)/(mid+soft) and hard colour as (hard-mid)/(hard+mid).

In additions to this, different types of flux-colour grids were attempted, which involved things such as plotting soft colour and hard colour versus total counts separately; plotting hard colour against hard+mid counts; soft colour against soft+mid counts; and normalized colour (hard-soft/hard+soft) against soft+hard counts. Furthermore, flux-flux plots were also considered. These plots involved plotting hard counts vs. soft counts, and were only generated for the reflection data.

These diagrams were applied to see if anything else could be included with colour-

colour diagrams in our analysis. This involved making parameter combinations and some models less difficult to distinguish between. It was also done to see if there were other methods that could be explored further with this type of analysis. In attempting to use these diagrams, it was seen that problems were seldom fixed, as lines for different parameter combinations were seen to still intertwine. The colour trends were also seen to be similar when using simulated data, so there was not any significant improvement in distinguishing between models. However, these plots should be considered in future studies to see if improvements can be made to fix this.

Chapter 3

COMPARISONS WITH DATA

3.1 ASSESSING SIMULATED DATA

To assess the use of these grids, the three reflection grids were tested with three simulated data sets done for the different combinations of variable parameters. These were generated by another party in order to avoid any bias in the data and were done using the "relxill" model and folding it through the same XMM response.

For a single data set, the values for the points in colour-colour space were first extracted as counts in the three bands along with their errors. With each combination of parameters tested, twenty pairs of parameter values were randomly generated between the maximum and minimum values used to create the grids. From this, the count rates and their errors were gathered as would be done for real data. As usual, the colours are found from these count rates and then plotted against each other. Error bars are included alongside them by using Gaussian error propagation to first calculate the uncertainties for the colours.

Here, we use Data Set 1 to denote the data with varying $\log(\xi)$ and Γ , Data Set 2 to denote the data with varying R_f and Γ, and Data Set 3 to denote the data with varying R_f and $\log(\xi)$. This offered the ability to study how effectively

reflection in AGN could be distinguished in colour-colour space. This is an important consideration, as reflection, absorption, and Compton scattering are the three main emission-related processes we have seen in AGN. Thus, difficulties identifying any of these could pose problems when trying to use these diagrams to better assess the internal AGN processes.

Data were first compared with Grid 5, as shown in Figure 3.1. All three data sets are seen to be well contained on the grid, with no points lying off of it. On this grid, Data Set 1 follows a very narrow track, with significant variations in Γ, but only very little in R_f (values around 0.5 to 1.5), thus, it appears to be mostly constrained in reflection fraction. Data Set 3 has the least spread in points compared to the other grids, as it stays around Γ=1.6 to Γ=2.2 and varies all across R_f. When looking at Data Set 2, it is clear that it has the largest spread of points in colour-colour space. It is noticed that the data varies largely along both the Γ and R_f tracks. There seems to be a minimum of Γ=1.2 and a maximum somewhere between Γ=2.8 and Γ=3.0. Reflection fraction varies from $R_f = 0.5$ to $R_f = 5.0$ for Data Set 2 on this grid. Having each of these data sets fit on this grid confirms that at least one of these parameters is varying for each data set, as expected. However, this does indicate to us that there can be some difficulty distinguishing between the appropriate parameter variations in certain instances. We do see that the most variable data set when compared to Grid 5 is Data Set 2, so its parameters fit best with both Γ and R_f varying. As such, this confirms the parameter variability for which Data Set 2 was generated.

We next compared data with Grid 6, as in Figure 3.2. Here it is clear that two of

the data sets, both Data Set 1 and Data Set 2, extend way past the grid with many points not lying on it at all. These two data sets are then not very fitting for the parameter variations seen in Grid 6. Data Set 3 is seen to be a lot more compact in colour-colour space, with a lack of large-scale variation in colours. As such, the data set is seen to fit perfectly on the grid, with not a single point lying off of the grid. The scatter in the points on this grid in many different directions shows that both parameters on the grid are indeed varying in some way. In fact the parameters are seen to vary from R_f=0.0 to R_f=5.0 and $\log(\xi)$=0.0 to $\log(\xi)$=3.0. With this data set appearing to visually fit well with Grid 6, we have reasonable evidence that this explains the appropriate parameter variations. This result confirms the parameter variations for which this data set was generated for, as it fits with the varying reflection fraction and ionization.

Lastly, data were compared with Grid 7, which can be seen in Figure 3.3. On this grid, both Data Set 2 and Data Set 3 have many points that clearly lie off of the grid, meaning that the grid does not fit their parameter variations well. Comparatively, Data Set 1 is well contained on the grid and is shown to have a lot of scatter in the points, with both Γ and $\log(\xi)$ varying across nearly their entire range. Two or so data points can be seen to be just over the edge of the grid, but error bars indicate that they still fit with the grid overall. This set of data has a wider spread across this grid then was found with Grid 5, indicating that the data is undergoing more variability when applied here. Even though it visually appears to fit well on both this grid and Grid 5, the higher variability here confirms the parameter variability used for Data Set 1.

Through testing the data on the grids developed for other models (i.e., the absorbed power law and partial covering models), it can be seen the most, if not all, of the points lie off of the grids. This is an indication that these models do not fit the data developed for the relativistic blurred reflection model. It is, thus, seen here that the data can be distinguished between different models. Importantly, it can be noticed with the absorbed power law grid that Grid 1 and Grid 2 (the two grids that have varying Γ) both seem to still follow a track of varying Γ even with the data largely lying off of the grid. This should indicate that the lack of a well-defined fit on these grids means that it is a result of the model and not the parameter variations. Thus, this provides some reasonable evidence that these grids can distinguish between models; all that remains is to assess with real data.
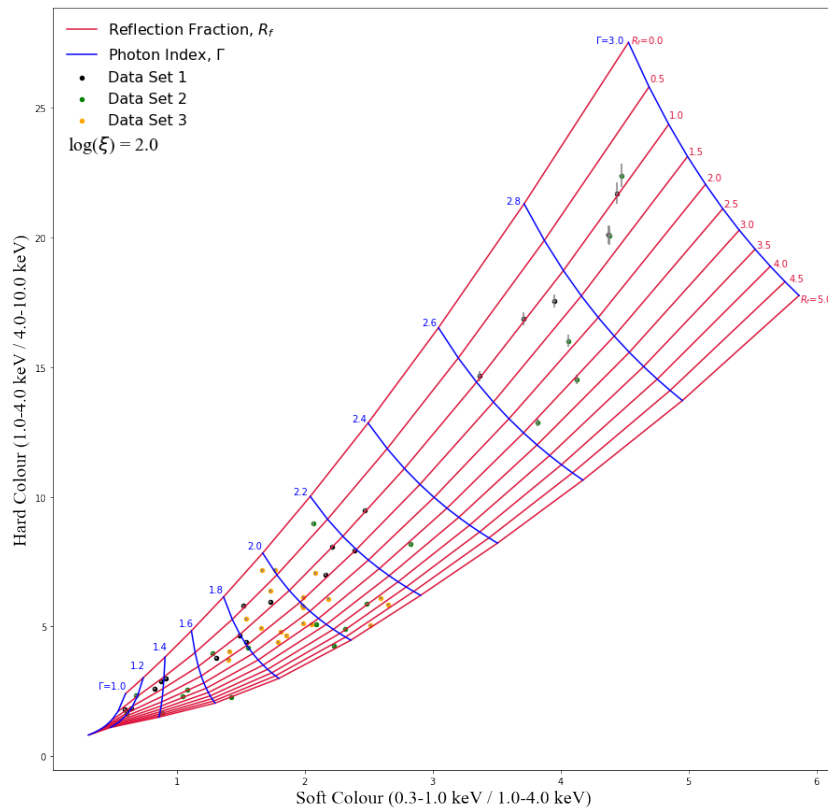

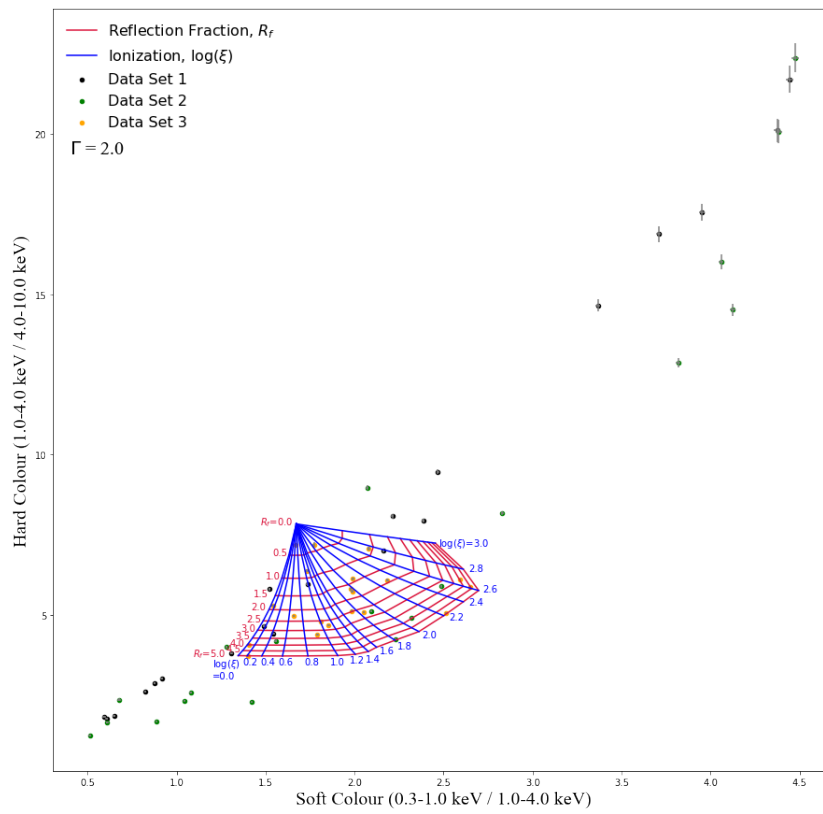Figure 3.1: Comparison of the three simulated data sets to Grid 5.

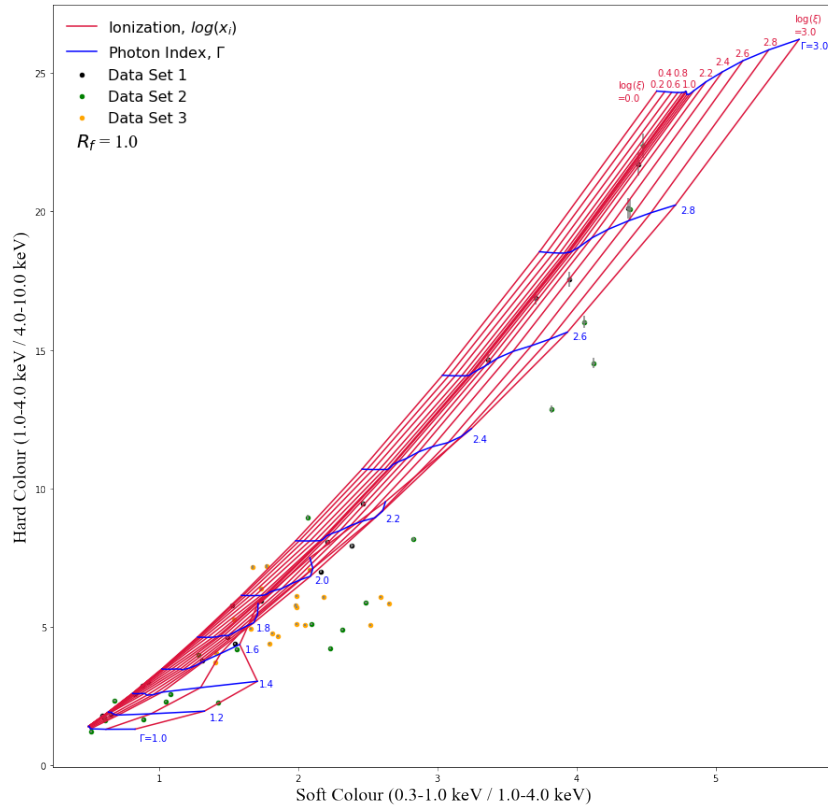Figure 3.2: Comparison of the three simulated data sets to Grid 6.

Figure 3.3: Comparison of the three simulated data sets to Grid 7.

3.2 ASSESSING REAL DATA

While tests with simulated data did show some promising results, it is useful to consider testing real data to identify that problems would be present. For the purposes of this work, data were taken from an April 2016 observation of NGC 6814, a Seyfert 1.5 galaxy, using XMM-Newton's EPIC detectors in large-window mode. These data were used in Gallo et al. (2021) and have already been processed, as normal with the XMM-Newton Science Analysis System (SAS), to "clean" the data and produce calibrated event lists. These were used to construct light curves, with the data binned with 1000s intervals, which were done in the three bands and used to extract count rates and their uncertainties. The data given to me were then used to find the colours

as usual, and these colours were plotted against each other and overlaid on each of the seven grids. The uncertainty on the count rates was used to calculate uncertainty in the colours by using Gaussian error propagation and then plotted with the data as error bars. Predictions of the variability in NGC 6814 were made based on the trends of the data and were compared to analysis already done on the object in Gallo et al. (2021).

The first comparison done was with Grid 1, the absorbed power law, and this is shown in Figure 3.4. As seen, the data were contained within one small corner slightly off of the grid, placing it close to $\Gamma=1.0$ to $\Gamma=1.4$ and $N_H=0.01\cdot10^{22}$ cm^{-2}. With most of the points falling off the grid, it indicates the model does not fit the data. An appropriate value for the galactic column density for NGC 6814 was determined to be around $N_H=1.53\cdot10^{21}$ cm^{-2} (Gallo et al., 2020). On the grid, this would be expected to be found between $N_H=0.1179\cdot10^{22}$ cm^{-2} and $N_H=0.1931\cdot10^{22}$ cm^{-2}, but that is not the case here. We can see that the real data does have a slight upward trend in both colours which, even with its column density, would point towards increasing Γ, but only slightly between $\Gamma=1.0$ and $\Gamma=1.4$. Thus, even though it does not lie on the grid well, it is likely that this is constrained to a constant column density. The grid, however, could not be used to extract much useful about NGC 6814, which might be an indication that this model in its current state is not a good description for the object.

With the first of the partial covering grids, Grid 2, which is seen in Figure 3.5, we can see that all of the points now lie on the grid. Very little movement is seen along the blue lines, which is the direction along which the ionization varies. This indicates

that, with the model in its current state, the source does not undergo much variation in ionization, if any. Variation is seen along the red lines, where absorber column density varies between N_H=7.1969·10^{22} cm^{-2} and N_H=1.9307·10^{22} cm^{-2}. It appears the data could be described well by changes in column density and slight changes in ionization.

The second of the partial covering grids, Grid 3, compared with the real data is seen in Figure 3.6. This is another grid that contains most of the data points, which is quite promising. On top of this, we see that the data very clearly follows one of the tracks quite well, which is seen as it goes along the red line at f_c=0.95. In fact, the points are seen to vary only slightly in covering fraction with the current grid. The ionization is frozen to $\log(\xi)$=1.0, which would likely need to be changed to fit with NGC 6814. Again, it appears that changes could be predominately due to varying column density.

The third of the partial covering grids, Grid 4, when compared with the real data is seen in Figure 3.7. This is the only partial covering grid for which most of the points are not on it. Even so, the points can be seen to vary in colour in such a way that indicates changes in covering fraction (only between f_c=0.90 and f_c=0.80) and just slight changes in ionization. Noting that the points lie well on two of the three grids, this model currently looks to be the most promising one for describing some of the variability in NGC 6814.

In Figure 3.8, we can see the first of the reflection grids, Grid 5, being compared to the real data. The data were seen to be constrained to the bottom of the grid, with point that vary between the first and third blue lines. This indicates a very

slight variation in photon index between $\Gamma=1.0$ and $\Gamma=1.4$. There is also a noticeable spread in the data points over multiple of the red lines. Thus, this diagram seems to be showing that the data exhibits some variability in reflection. Since we have a somewhat arbitrary constrained ionization, this could change when adjusting the values unless it is found that this is the appropriate value. The variation of Γ values is consistent with what we saw when comparing the data to Grid 1. However, we note that $\Gamma < 1.7$ is uncommon in AGN. Such flat photon indices may be nonphysical.

Figure 3.9 shows the second of the reflection grids, Grid 6 compared to the real data. Here, the data were seen to lie way off of the grid, further than with any of the other grids. The diagonal trend we see in colour is, however, consistent with varying reflection fraction and relatively constant ionization. This is consistent with previous trends we have noticed in other comparisons. Reflection fraction is seen to vary more on these grids than is seen in Gallo et al. (2021), as they had seen a relatively constant reflection fraction.

Grid 7, the third of the reflection grids, is seen being compared to the real data in Figure 3.10. The points are seen to vary over the blue lines slightly, indicating again that the photon index is varying between $\Gamma=1.0$ to $\Gamma=1.4$. These points are pointed more vertically (i.e., more of a change in hard colour), indicating there to be little variation in the ionization. Once again, since we found slight variability in reflection fraction, different constrained values for that parameter should be tested and analyzed for how the positions change. Again, as in the case with Grid 5, the low values predicted for Gamma are unusual and may rule out this model.
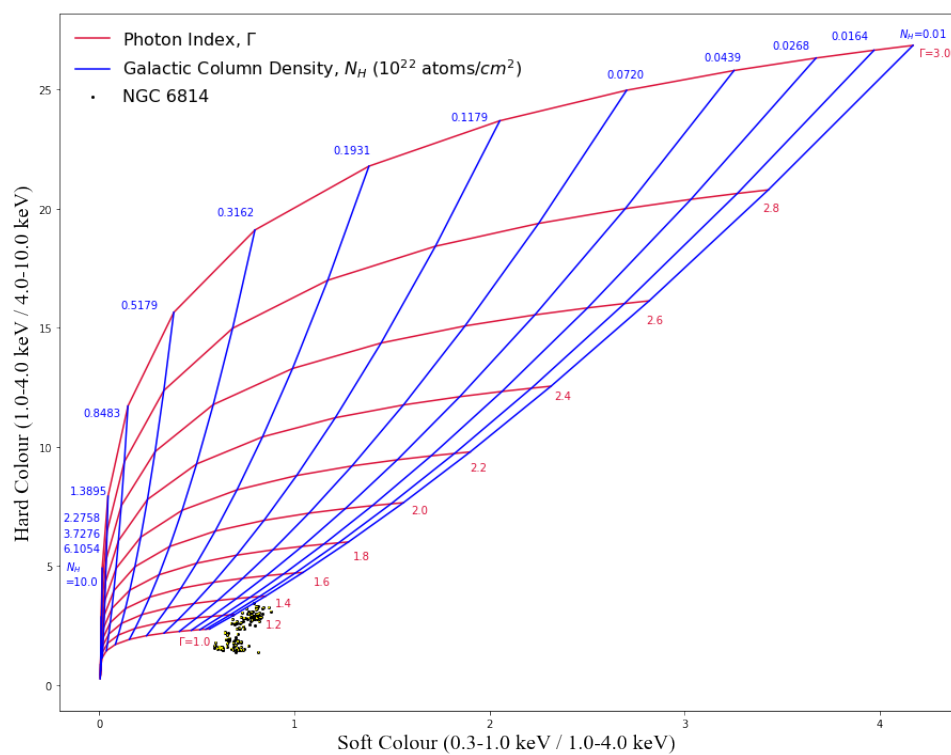
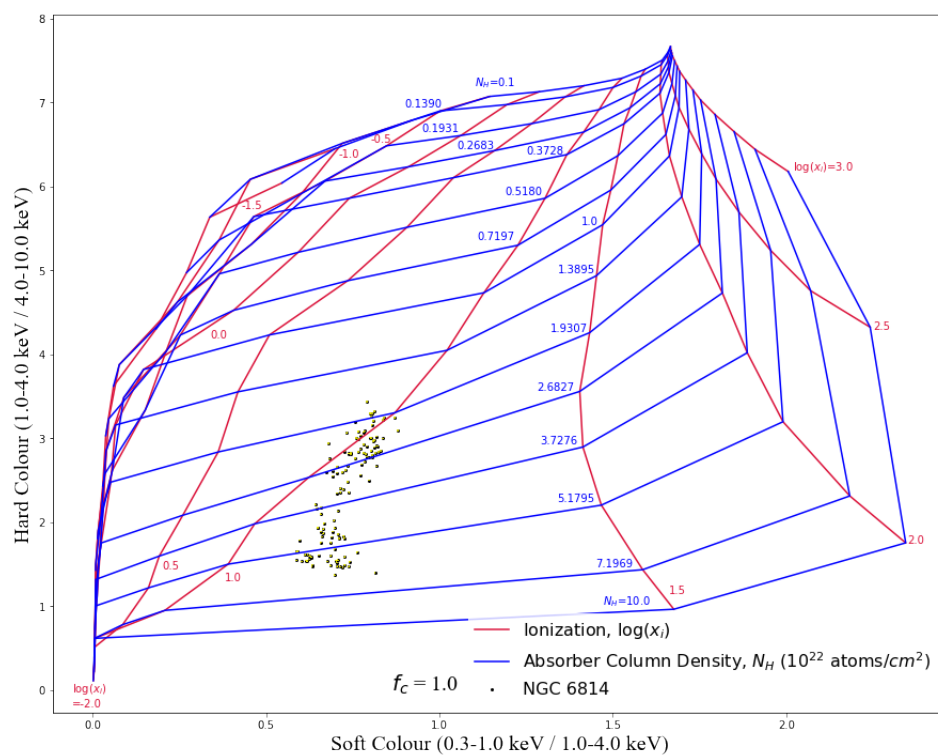Figure 3.4: NGC 6814 data in colour-colour space overlaid on Grid 1.

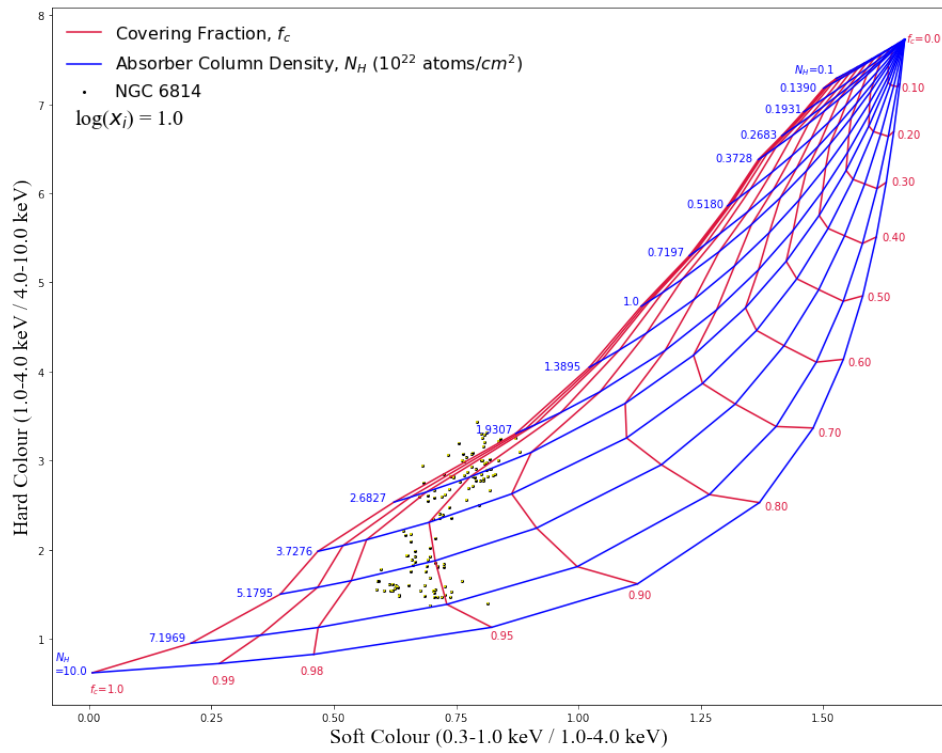Figure 3.5: NGC 6814 data in colour-colour space overlaid on Grid 2.

Figure 3.6: NGC 6814 data in colour-colour space overlaid on Grid 3.
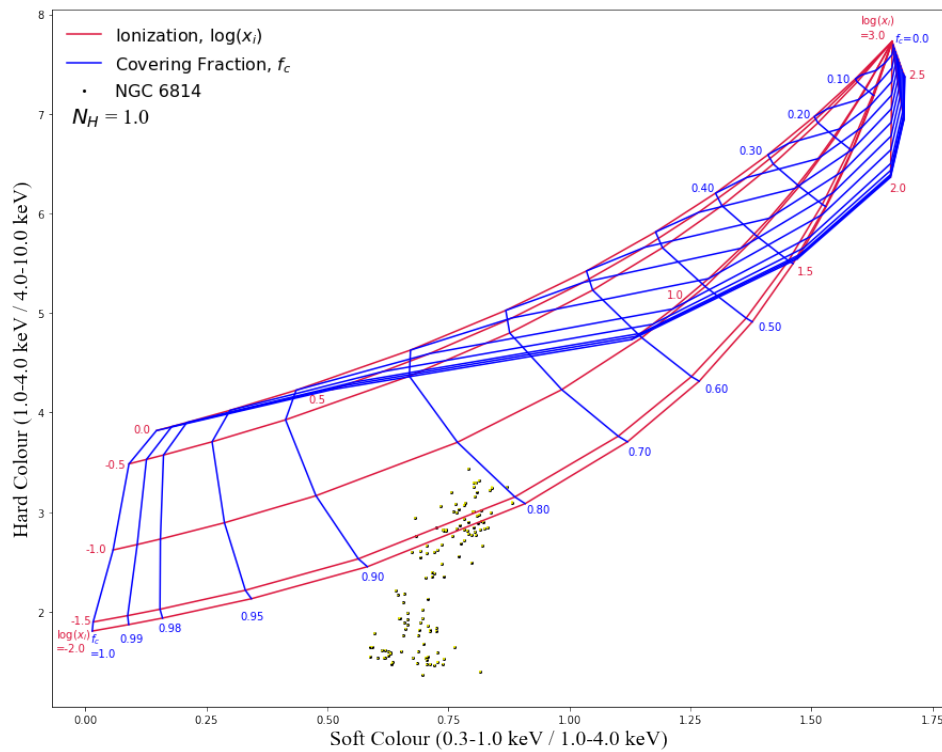

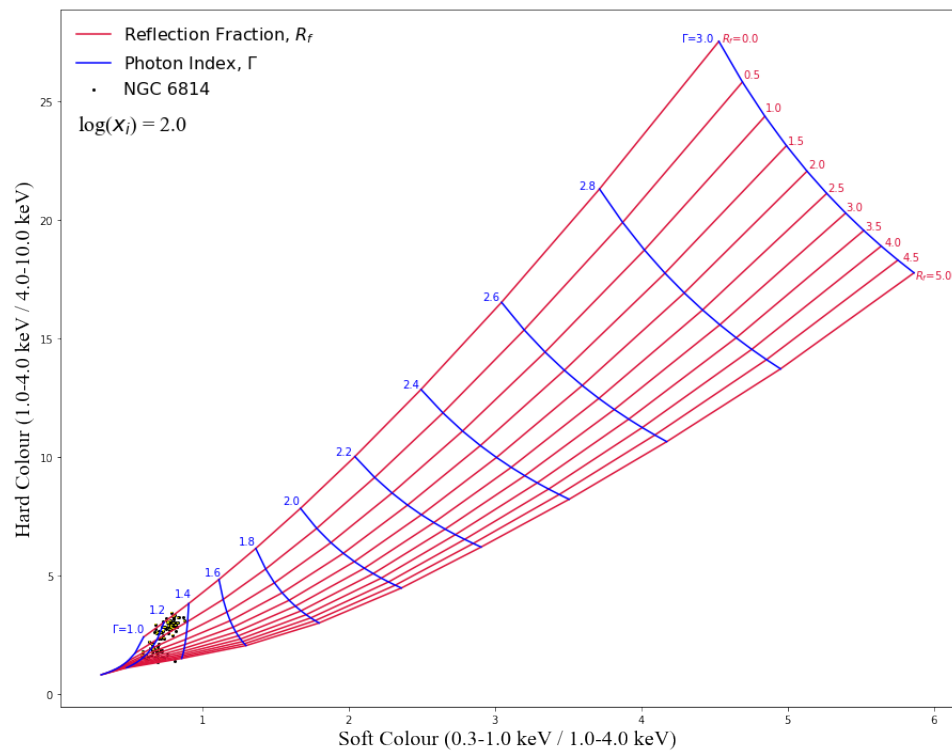Figure 3.7: NGC 6814 data in colour-colour space overlaid on Grid 4.

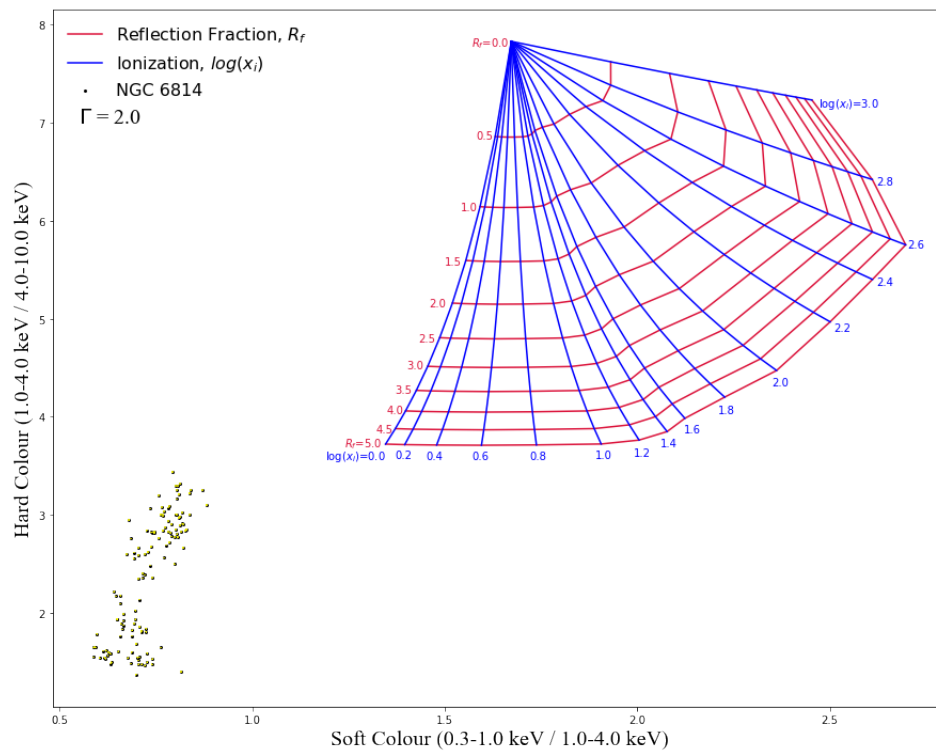Figure 3.8: NGC 6814 data in colour-colour space overlaid on Grid 5.

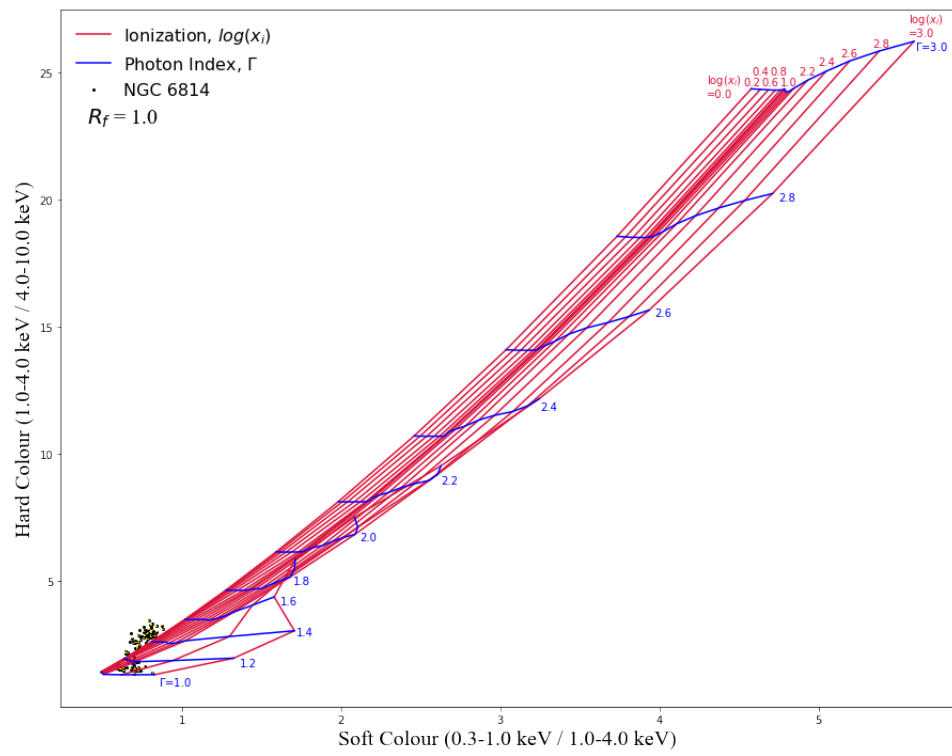Figure 3.9: NGC 6814 data in colour-colour space overlaid on Grid 6.

Figure 3.10: NGC 6814 data in colour-colour space overlaid on Grid 7.

Chapter 4

DISCUSSION

Considering the simulated data, it was seen that Data Set 1 fit well onto both Grid 5 and Grid 7. This indicates that ionization and reflection can be difficult to distinguish. Comparisons with Data Set 2, however, did not encounter the same problem, leading us to believe that it might not be the central issue here. It is important to note that, even though both grids fit well, the proper one was seen to exhibit more variability. Thus, it would be likely that, in the case of two difficult to distinguish parameters, the appropriate changes can be seen by which parameters undergo the most significant variability. In the case of real data, one could make the prediction that this could cause issues identifying the true variable parameters and maybe also the appropriate model, as it is likely that variability could occur in other parameters. The fact that the data set that is supposed to show reflection variability also shows a small amount of ionization variability, makes it seem like there is a potential connection between the two parameters. This is one thing that future work could analyze.

Applying the colour-colour grids to NGC 6814 data showed some promising results, but it still needs some significant improvements. To assess the accuracy of these grids, the results of our comparisons were compared to the results found in Gallo et al. (2021). In this paper, the most acceptable result was for when covering fraction was left to vary, and all the other parameters, such as absorber column density, absorber

ionization, reflection fraction, etc., are found to be constrained. Further, the most

fitting model, with all this in mind, was a non-variable ionized blurred reflection

continuum covered by a variable partial covering. There was also some noticeable

variability in column density, especially for the warm absorber. When comparing this

to what we found with the grids, it is seen that the results are somewhat consistent.

Our tests found column density of a partially covering observer to be the most varying

parameter, which is not consistent with NGC 6814, however, it does confirm the

variability of absorption in some form. Thus, it seems to have been able to pick

out absorption variability. We noticed slight variations in covering fraction, but not

enough to be consistent with this paper, as they noted it as varying from around

f_c=0.0 to f_c=0.56. The constrained ionization noticed from our grids is consistent

with the paper as well, for both the disk and partial coverer. Noticing that the data

points seemed to be somewhat contained on the partial covering and blurred reflection

grids, this likely indicates that the grids are consistent with the paper. We have seen

slight variations in reflection fraction and covering fraction, as well as with photon

index, but not enough to be considered significant. Thus, it could be considered

roughly constant when compared to the paper. It is clear that these diagrams are

quite promising for exploring AGN X-ray variability. These comparisons to NGC

6814 data have given clear indications that more can be done to modify the grids.

Chapter 5

CONCLUSION

As an attempt to break model degeneracies, we employed the use of colour-colour diagrams, an instrument-dependent tool. Using colours, ratios between the fluxes in three energy bands, grids with tracks indicating clear parameter variations were constructed. Both simulated data and real observational data of NGC 6814 were plotted alongside the grids and observations were made based on the tracks the data carved out in colour-colour space. Conclusions were then drawn from comparisons of these tracks to the seven grids generated from the three different models: absorbed power law, partial covering, and relativistic blurred reflection.

With colour-colour grids constructed, trends were seen in soft and hard colours as different parameter tracks were traversed. These trends were determined to be mostly consistent with what should occur within an AGN environment. Some problems were noticed, however, when attempting to distinguish between reflection and ionization in the simulated data, but this issue was only seen to come up once overall. There was little difficulty identifying photon index variability in all of the simulated data grid comparisons. These grids were also seen to be distinguishable between models, as the simulated data sets only worked well with reflection, being completely off for every other model.

The grids were not edited before testing real data because it allowed for us to

understand the effects of different parameters on data to assess what improvements would likely need to be made. Adding host-galaxy column density to all the models was attempted, but it alone was found to not improve how well the data and grid matched up. This indicated that more components and detail should be applied to these grids, such as the use of a warm absorber.

Grid comparisons showed that variations in absorber column density gave the best description for NGC 6814, with no variation seen in ionization and very little seen in every other parameter, including covering fraction. Some of this is in contrast to what has been seen to actually vary for NGC 6814, as covering fraction has generally been determined to be the most variable parameter. It is likely, though, that it could be found to be more consistent when taking into account the warm absorber known to be present. On top of this, indications are that further constraints, that make it more fitting to NGC 6814, are needed to improve the results. Flux-flux plots and flux-colour plots were also employed, but were found to pose no significant advantage when used in conjunction with the colour-colour grids.

The X-ray variability in AGN is partially identified by using colour-colour grids. It is, however, found that grids constructed from simple models cannot alone describe this variability. This makes it likely that more complicated grids need to be constructed that take into account various components known to exist around the AGN environment, such as warm absorbers, and galactic absorption.

Future work would improve upon the results presented so far. General tests that should be done are to modify some of the frozen parameters and see how the grid appearance changes. This should include constructing one-parameter grids for the

various non-varying parameters to make predictions to how they modify the grids. It is known that NGC 6814 has warm absorbers present, so future studies on this topic would include this component by using the "warmabs" model in *xspec*. Along with this, it has a known constrained galactic column density of $1.53 \cdot 10^{21}$ cm^{-2}, so this will be taken into account in the future. These applications will also be done on other sources, if this route is chosen in the future.

There are many future applications for these grids, once they are eventually found to be successful at assessing AGN variability. Grids can be generated for a large number of sources at a time and be used to analyze their various properties. It is, thus, the hope that future studies would allow for a much greater understanding of the AGN environment and geometry of the various components.

Bibliography

1. Blandford, R., Meier, D., Readhead, A., 2018, Annual Review of Astronomy and Astrophysics, 57, 467

2. Carpano, S., Wilms, J., Schirmer, M., Kendziorra, E., 2005, A&A, 443, 103

3. den Herder, J. W., Brinkman, A. C., Kahn, S. M., Branduardi-Raymont, G., Thomsen, K., et al. 2001, A&A, 365, L7

4. Dong, Y., Garcia, J. A., Liu, Z., Zhao, X., Zheng, X., Gou, L., 2020, MNRAS, 493, 2178

5. Ehler, H. J. S., 2019, MSc Thesis, Saint Mary's University

6. Ehler, H. J. S., Gonzalez, A. G., Gallo, L. C. 2018, MNRAS, 478, 4214

7. Fabian, A. C., Rees, M. J., Stella, L., White, N. E., 1989, MNRAS, 238, 729

8. Gallo, L. C. 2011, JRASC, 105, 143

9. Gallo, L. C., Gonzalez, A. G., Miller, J. M., 2021, ApJL, 908, Issue 2

10. Gallo, L. C., Grupe, D., Schartel, N., Komossa, S., Miniutti, G., Fabian, A. C., Santos-Lleo, M. 2011, MNRAS, 412, 161

11. Gaur, H., Gu, M., Ramya, S., Guo, H., 2019, A&A, 631, A46

12. Gonzalez, A. G., Wilkins, D. R., Gallo, L. C. 2017, MNRAS, 472, 1932

13. Grinberg, V., Nowak, M. A., Hell, N. 2020, A&A, 643, A109

14. Jansen, F., Lumb, D., Altieri, B., Clavel, J., Ehle, M., Erd, C., Gabriel, C., Guainazzi, M., Gondoin, P., Much, R., Munoz, R., Santos, M., Schartel, N., Texier, D., Vacanti, G., 2001, A&A, 365, L1

15. Kara, E., Fabian, A. C., Lohfink, A. M., Parker, M. L., Walton, D. J., Boggs, S. E., Christensen, F. E., Hailey, C. J., Harrison, F. A., Matt, G., Reynolds, C. S., Stern, D., Zhang, W. W., 2015, MNRAS, 449, 234

16. Lumb, D. H., Schartel, N., Jansen, F. A., 2012, Optical Engineering 51(1), 011009

17. Nowak, M. A., Hanke, M., Trowbridge, S. N., Markoff, S. B., Wilms, J., Pottschmidt, K., Coppi, P., Maitra, D., Davis, J. E., Tramper, F., 2011, ApJ, 728, 13

18. Petrucci, P.-O., Ursini, F., De Rosa, A., Bianchi, S., Cappi, M., Matt, G., Dadina, M., Malzac, J., 2018, A&A, 611, A59

19. Tanaka, Y., Boller, T., Gallo, L., Keil, R., 2004, PASJ, 56, L9

20. Willingale, R., Starling, R. L. C., Beardmore, A. P., Tanvir, N. R., O'Brien, P. T., 2013, MNRAS, 431, 394

21. Yang, Q., Xie, F., Yuan, F., Zdziarski, A., Gierlinski, M., Ho, L. C., Yu, Z., 2015, MNRAS, 447, 1692

22. Zackrisson, E., 2005, https://www.diva-portal.org/smash/get/diva2:166557 /FULL-TEXT01.pdf